DEVELOPMENT AND VALIDATION OF A LAMINAR NUMERICAL WAVE TANK FOR FLOATING BODY MOTION STUDY

A Thesis

by

YIJUN SUN

Submitted to the Graduate and Professional School of
Texas A&M University
in partial fulfillment of the requirements for the degree of

MASTER OF SCIENCE

Chair of Committee,	Mirjam Fürth
Committee Members,	Björn Windén
	Orencio Durán Vinent
	Edward White
Head of Department,	Sharath Girimaji

August 2022

Major Subject: Ocean Engineering

ABSTRACT

Numerical simulations have been routinely applied in marine design for the past decades. The limitations of this approach lie in the requirement of high computational power and the development of computer technologies especially in the pre and post processing. For some numerical schemes, the computation cost can be very high. However, with rapid development in computational capability in recent years, these limitations are slowly vanishing. Many simulation schemes for modeling turbulent flow have been developed such as Reynolds-Averaged Naver Stokes (RANS) and Partially Reynolds-Averaged Navier Stokes (PANS). RANS methods can generate precise simulations for flows with small scale turbulence at an acceptable computational cost. However, due to the limitation in distinguishing large and small scale motion, this method is not suitable for large scale turbulence. While PANS methods can solve both large and small scale turbulence, the computational cost is higher compared to RANS methods. In this research project, numerical wave tanks with a heaving buoy using laminar simulations are presented to study the complex motions in an incompressible two-phase flow . The simulations are generated using the interFoam solver, which is embedded in OpenFOAM and provides solutions to multiphase incompressible flow with optional mesh motion. The main outcomes of these simulations are time series of waves measured at upstream and downstream of the buoy and the the buoy response motions. The results of these simulations are compared to previous experiment as well as numerical RANS and PANS simulations conducted by other members of the Fürth Lab.

DEDICATION

This thesis is dedicated to my mother, Jing Wang (1967-2020) who was a believer in me and full supporter for my higher education goal, until cancer lead to her tragic passing in 2020.

ACKNOWLEDGMENTS

I would like to thank the Texas A&M University Graduate and Professional School allowing me to conduct this research project. And I would like to express my sincere gratitude to Dr. Mirjam Fürth for being the Chair of my committee, as well as Dr. Björn Winden, Dr. Orencio Durán Vincent, and Dr. Edward White for being my committee members, with all the valuable advice and guides provided.

Moreover, I would like to express my sincere appreciation to my father, Yong Sun, in his support and love during the course of this research study. I would also like to thank all my families for their support and care.

CONTRIBUTORS AND FUNDING SOURCES

Contributors

This work was supported by a thesis dissertation committee consisting of Professor Mirjam Fürth, Professor Björn Winden, Professor Orencio Durán Vinent of the Department of Ocean Engineering, and Professor Edward White of the Department of Aerospace Engineering.

A previous physical experiment, to which the numerical simulation results are compared for validation, was conducted by the Fürth Lab members lead by PhD student Omar Khaled Ahmed Kamal Sallam of the department of Ocean Engineering. The control experiment was conducted by the author.

The RANS and PANS simulation in this research thesis was conducted by PhD student Ahmed Atef Abelsatar Ahmed Hamada of the department of Ocean Engineering.

Funding Sources

This graduate study was completed without outside financial support.

NOMENCLATURE

AWA	Active Wave Absorption
CAD	Computer-Aided Design
CDS	Central Difference Scheme
CFD	Computational Fluid Dynamics
CVS	Control Volume
FVM	Direct Numerical Simulation
IMU	Inertial Measurement Unit
KLT	Kanade-Lucas-Tomasi Algorithm
NWT	Numerical Wave Tank
OpenFOAM	Open-source Field Operation and Manipulation C++ toolbox
PANS	Partially Reynolds-averaged Navier-Stokes
PC	Personal Computer
PWA	Passive Wave Absorption
RANS	Reynolds Averaged Navier-Stokes
TVD	Total Variation Diminishing
VOF	Volume of Fluid Methods
WG1	Wave Gauge 1 at 3.16 $[m]$
WG2	Wave Gauge 2 at 4.53 $[m]$
VSLAM	Visual Simultaneous Localization and Mapping Algorithm

TABLE OF CONTENTS

Page

LIST OF FIGURES

FIGURE Page

LIST OF TABLES

TABLE Page

1. INTRODUCTION

Ocean waves show high potential in energy harvesting. Countless studies have been conducted in the field of marine science and engineering in order to understand more about wave propagation. Experiments conducted in physical wave tanks have long been used. However, these physical experiments are relatively expensive and time-consuming. In addition, physical testing has limitations due to tank size and wave maker performance.

1.1 State of Art and Limitations of Numerical Simulations

As an alternative approach, numerically simulated waves allow for a larger range of possible test cases. The basics of this approach is to describe the fluid flow with partial differential equations governing the conservation of mass, energy, and momentum of the fluid. This is known as Computational Fluid Dynamics (CFD). Under most circumstances, it is rather complicated to solve these equations analytically. With numerical simulations, the domain of interest is discretized into smaller sub-volumes called computational cells. The governing equations are solved in each of these cells and assembled (through the connectivity among the cells within the mesh) to represent the flow situation in the whole domain. Using numerical simulations, complicated problems in marine science and engineering can be studied by directly visualizing the simulation results using graphical and animation tools in the post-processing procedure. Moreover, many numerical simulation methods have been shown to be successful in assisting the understanding of complex hydrodynamics [17].

The success of the numerical modeling approach relies highly on the available computational power and properly designed numerical schemes. Some schemes result in high demand on the performance of computer processors. However, due to improved computational power in personal computers, complicated simulations that previously required supercomputers can now be operated

on personal computers (PC's) using parallel running processes which increases the availability of computational capabilities [17, 34, 33].

Numerical simulations of ocean waves introduce a further complication, the two-phase flow of water and air and the resulting free surface dynamics. The open source CFD suite OpenFOAM® has been widely used in marine applications for the last decades. The *interFoam* solver which is part of OpenFOAM® solves the continuity equation and Navier Stokes equations for two-phase incompressible, isothermal, and immiscible fluids. This solver is based on the Volume of Fluid (VOF) method [9].

1.1.1 Floating Body Dynamical Response

Many marine designs rely on their seakeeping performance, such as weather buoys, wave energy converters, and different types of vessels. In numerical simulations, the involvement of floating bodies introduces more complexity during the process due to the additional degrees of freedom. The floating body also induces reflected waves that increase the non-linearity in the wave propagation and dynamical response [3, 16].

Previous simulations show some inaccuracy in the estimate of dynamical responses even if the simulated wave fields are accurate compared to experimental and analytical results. These previous studies were all conducted with the involvement of different types of floating bodies (free fall wedge [16], rectangular barge [3], hemispherical float [26]) with some constraints in the degrees of freedom of the motion. For both studies conducted by [26] and [3], the simulations were performed using OpenFOAM® with similar Numerical Wave Tank (NWT) designs. In addition, the methods used for wave absorption are based on the same theoretical foundations as those presented in this thesis. The results from all three studies are validated and verified against a considerable amount of sources including physical experimental data and simulations from other researchers [26, 3, 16]. These results indicate some inaccuracies in the floating body motions; although the overall simu-

lation results show appreciable accuracy in wave properties compared to experiments. In addition, the execution time for the freely pitching hemispherical float by [26] significantly increased for larger scale motions of the structure.

1.2 Aims and Objectives

In this thesis, two different numerical simulations are conducted for a 2-phase incompressible laminar flow problem. The first simulation aims at building a NWT subject to a regular wave field. The second simulation, based on the first simulation, features the addition of a floating buoy in the wave field, constrained to heave motion only.

The simulations are conducted using the open source CFD suite OpenFOAM®. These laminar simulation results are compared to previous experimental data for validation. The comparison is made in terms of the surface elevation data from time series of waves, error analysis, and dynamical response of the floating body. Finally, the results from the laminar simulations are compared to simulations where turbulence is considered by using RANS and PANS methods.

The purpose of these two simulations lies mainly in two aspects. Firstly, by the difference regarding buoy involvement between the two simulations, the accuracy problem in Section 1.1.1 is reproduced and studied. With the surface elevation from the first simulation validated by physical experiment results, the accuracy of dynamical responses of the added buoy is evaluated. Moreover, possible solutions attempting to improve the accuracy problem will be proposed based on simulation results. Secondly, the results from these simulations are compared to results from other numerical schemes in terms of accuracy using almost identical numerical designs with additional evaluations on the balance between the desired accuracy level and the computational power cost.

2. THEORETICAL FOUNDATIONS

Since numerical simulations involve mathematically solving fundamental governing equations using computational tools, it is essential to briefly address the theoretical foundations including the turbulence theories, governing equations, wave theories, and surface capture methods involved before proceeding to the numerical simulation design.

2.1 Laminar and Turbulent Flows

Fluid flows can be divided into two different major types; laminar flows and turbulent flows. In laminar flows, the fluid flow has no disruption between different infinitesimal parallel layers. In other words, no lateral mixing is present between streamlines of the flow. On the other hand, turbulent flow is characterized by the random movement of particles. The transition from laminar flow to turbulent flow was first studied by Osborne Reynolds, who performed the classical experiments of flows in pipes. The dimensionless Reynolds number was defined in these experiments for characterizations of flows and can be computed as in Equation 2.1

$$Re = \frac{U L_C}{\nu} \tag{2.1}$$

where U is the velocity of the flow, L_C is the characteristic length, and ν is the kinematic viscosity of the fluid. [28].

2.2 The Continuity Equations and Naver Stokes Equations

The governing equations of laminar flow are the continuity equation for constant density:

$$\frac{\partial u_i}{\partial x_i} = 0 \tag{2.2a}$$

and the Navier-Stokes equations for incompressible flow:

$$\rho\left(\frac{\partial u_i}{\partial t}+u_j\frac{\partial u_i}{\partial x_j}\right)=-\frac{\partial p}{\partial x_i}+\mu\frac{\partial^2 u_i}{\partial x_j\partial x_j}+f_i \tag{2.2b}$$

where u_i denote the velocity components $[m/s]$ in a Cartesian coordinate system, ρ is the density of the fluid in $[kg/m^3]$, μ is the dynamic viscosity of the fluid in $[Pa.s]$, p is the pressure in $[Pa]$, and f_i represents the external body forces acting on the fluids (in this case, $f_i = 0, 0, \rho g z$ respectively in x-, y-, and z-directions, where g is the gravitational acceleration, set to -9.8 $[m/s^2]$ [18].

2.3 The Volume of Fluids Method (VOF)

The Volume of Fluid (VOF) method was first introduced by [14] whereby the phase interface between different fluids is represented as the fractions of liquid volume α in each cell during the simulation [27]. In the simulations presented in this thesis, this method is utilized in order to track the dynamics of the free surface. The volume fraction between water and air are determined in each cell, which is achieved by solving:

$$\frac{\partial\alpha}{\partial t}+\vec{U}\cdot\nabla\alpha=0 \tag{2.3}$$

The density and the dynamic viscosity are computed with the addressed phase fraction using the following equations:

$$\rho=\alpha\rho_w+(1-\alpha)\rho_a \tag{2.4a}$$

$$\mu=\alpha\mu_w+(1-\alpha)\mu_a \tag{2.4b}$$

where ρ is the density of the mixture of fluid in the selected grid cell with ρ_w and ρ_a being the density of water and air, respectively. μ represents the dynamic viscosity, with μ_w being the dynamic viscosity of water and μ_a being the dynamic viscosity of the air. The α in both Equations 2.4a and 2.4b represents the phase fraction.

Figure 2.1 is an illustrative example of the VOF method to determine surface fluid features. According to the VOF method, the phase fraction of a cell is 1 when it is fully submerged in water, and 0 when it is fully in air. When a cell is in a region with an air-water mixture, the phase fraction α ranges from 0 to 1 based on the true phase fraction in the cell [8, 22]. Additional information of applications and development of the VOF method can be found in the work of [24] and [14].

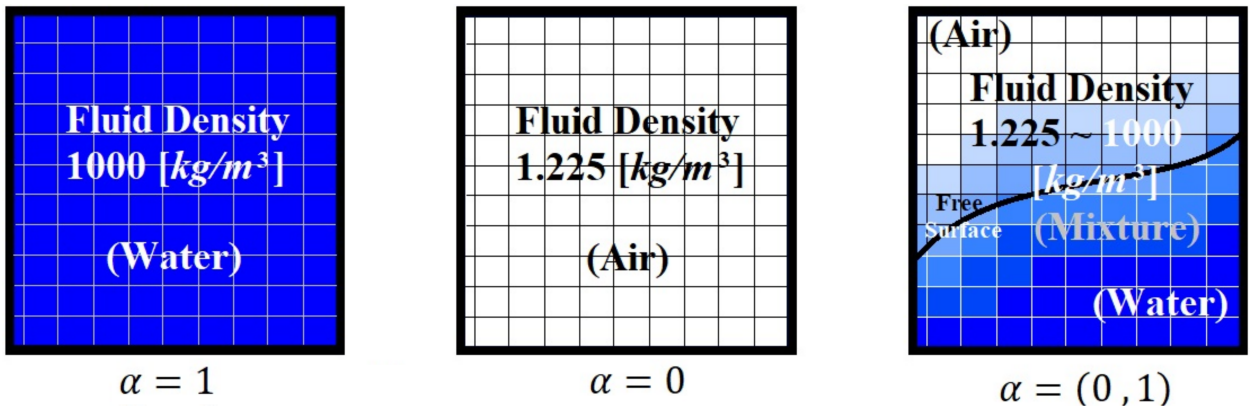

Figure 2.1: VOF phase fraction representation. The value of 1 represents cells full of fluid with density of 1000 [$kg.m^{-3}$] (water), while the value of 0 represents cells full of fluid with density of 1.225 [$kg.m^{-3}$] (air). Numbers between 0 and 1 indicates cells full of fluid with density between 1.225 and 1000 [$kg.m^{-3}$] (mixture).

2.4 Wave Theory

In order to provide a consistent basis for comparing waves in the physical experiment and the numerical simulations, the wave period, wave height, and water depth were analyzed to determine the wave regime. A MATLAB function was built based on the work of [20] that solves the dispersion relation 2.6a. This function was used for the identification of wave parameters in this simulation. With the depth of water being 0.38 [m], wave period being 2 [s], and wave height being 0.047 [m] as was used in Appendix A, the wavelength L and wave number k_n are calculated as 3.6123 [m] and 1.7394 respectively. Figure 2.2 shows the result from the wave categorization where x- and y-axes represent the relative depth and relative height respectively. Here, the waves

are Stokes 2^{nd}-order wave in transitional water as indicated by the blue dot in Figure 2.2.

The Stokes 2^{nd}-order wave theory describes regular progressive waves with nonlinear features [6]. The free surface elevation can be expressed as:

$$\eta = \frac{H}{2}\cos(k_n x - \omega t) + \frac{H^2 k_n}{16}\frac{\cosh(k_n h)}{\sinh^3(k_n h)}(2 + \cosh(2k_n h))\cos(2(k_n x - \omega t)) \tag{2.5}$$

where H is the wave height and h is the water depth. ω is the frequency of the wave, k_n is the wave number, and λ is the wavelength, these terms are defined by:

$$\omega = \sqrt{g k_n \tanh(k_n h)} \tag{2.6a}$$

$$k_n = \frac{2\pi}{\lambda} \tag{2.6b}$$

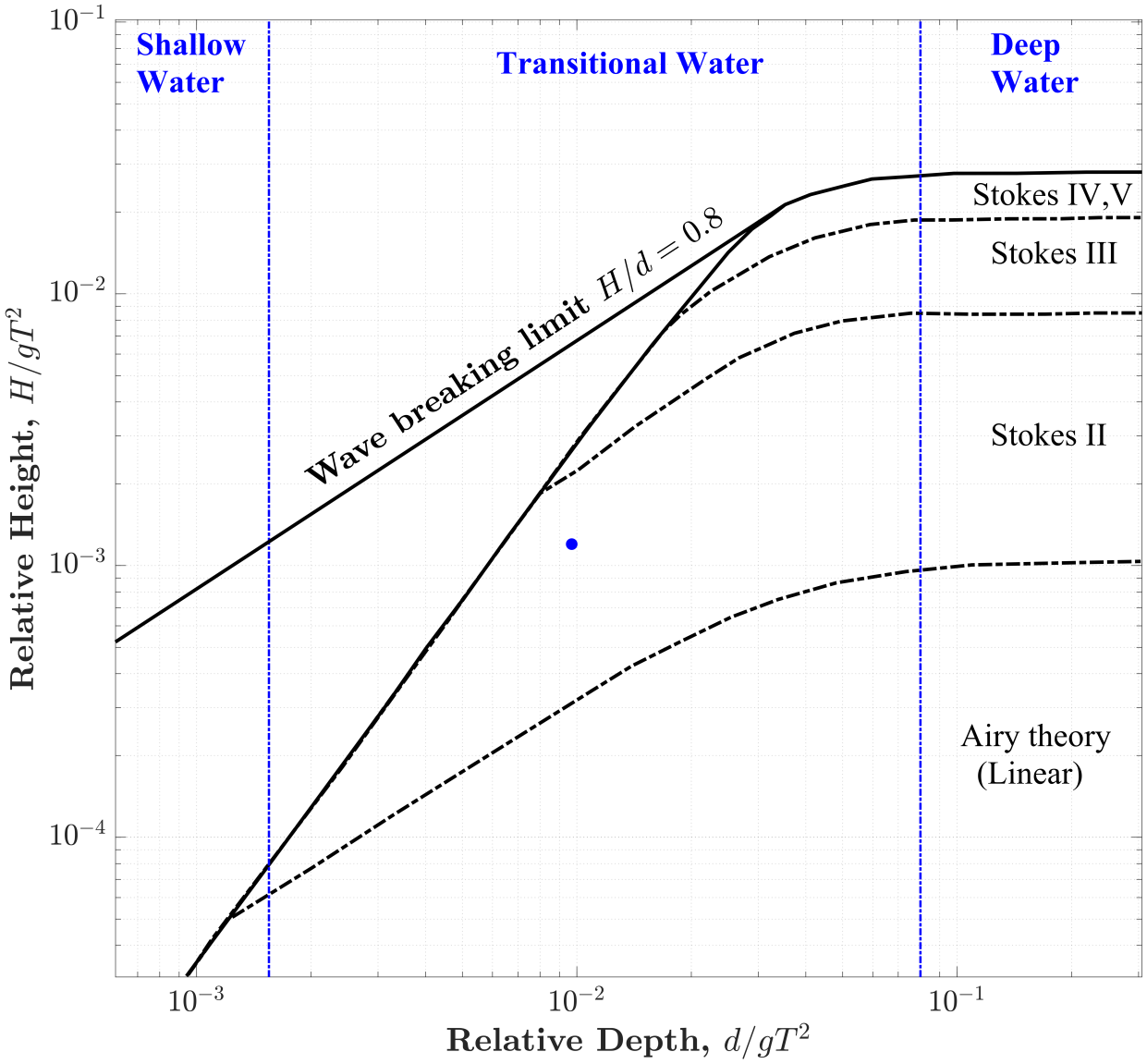

Figure 2.2: Stokes Second-order wave identification. The simulated wave is marked with a blue dot. The base plot is divided into parts closed by border wave conditions of different types [20].

3. PHYSICAL EXPERIMENT

An experiment (Experiment 1) was conducted in an Armfield wedge-style wave tank for regular wave generation located at the Haynes Engineering Building of Texas A&M University, College Station campus. The wave tank is 11.25 [m] long and 0.6 [m] in width and depth. The still water level was set at 0.38 [m]. A resistance type wave gauge was installed at 3.16 [m] from the upstream end of the tank for surface elevation measurements. In order to eliminate possible errors disqualifying results for validation of wave fields, this experiment was conducted excluding the buoy; resulting in solely regular wave fields. In addition, a prism shaped permeable beach with a height-base ratio of 0.6 [m]:1.2[m] was installed at the far end of the wave tank to account for wave absorption in avoidance of reflection waves reaching the wave gauge and contaminate the surface elevation signals. The period of the waves generated in this experiment is set by a dial number of 3.5 on the wave maker controller, which correspond to the wave period being 2 [s].

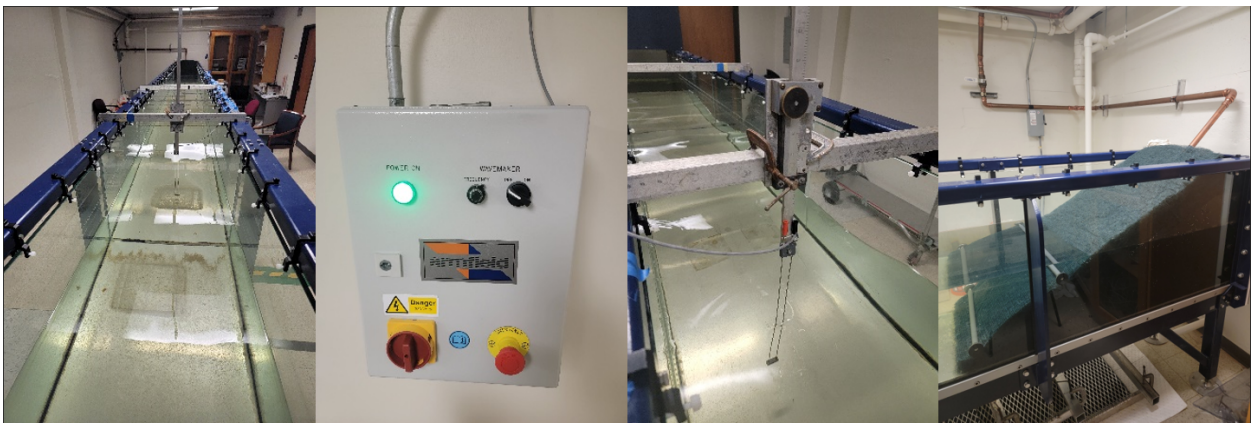

Figure 3.1: From the left: first image showing the top view of the tank; second image showing the wave maker controller; third image showing closer view of the wave gauge with tapes and foam stripes to fix the wires from the gauge to reduce vibrations; fourth image showing the prism shape permeable beach accounting for wave absorption at far end of the tank

Figure 3.1 shows some images taken during this experiment. The first image from the left shows the top view of the majority portion of the wave tank used in this experiment. The second

image displays the wave maker controller with the dial number knob and power switches. The thrid image shows the closer view of the wave gauge installed for surface elevation measurement. Some tapes and foam stripes were used to both fix the wires from the wave gauges and reduce the vibrations during the experiment to avoid high level of noise contaminating the signals. The signals are connected to a measurement station and once connect to PC's the signals can be visualized using the data acquisition application in MATLAB toolbox. The fourth image shows the prism shaped permeable beach for wave absorption.

4. NUMERICAL MODEL

The numerical solver used for these simulations was *interFoam*, which is part of OpenFOAM®. The *interFoam* solver solves the Continuity equations 2.2a and Navier Stokes equations 2.2b for two incompressible, isothermal, and immiscible fluids. This solver is based on the VOF method as was described in Section 2.3.

4.1 The *interFoam* Solver

[7] evaluated the performance of the *interFOAM* solver. They analyzed the interface capturing methodology in a variety of different perspectives and situations, including the accuracy in interface representation, mass conservation, implicit interface capturing for spurious currents, and the capability in problems with large density ratios. Some accuracy issues with the solver were found, including large disparity between local truncation and global error, mismatch to analytical prediction in curvature computation for a verification test involving stationary 2D droplet. However, these issues are deemed to be of minor effect in this case. Overall, the *interFoam* solver is shown to be capable on a wide range of flexible mesh options as well as turbulence modelling options that can be customized for different simulations. [7] also presented a review of recent multiphase flow studies using the *interFOAM* solver. For instance, regarding problems of floating body in fluid domains, they mention that [22] performed analyses of velocity data for flows around a cylindrical floating body. With comparison to experimental data, the results from the numerical simulation using the *interFOAM* solver are shown to be accurate.

4.2 Numerical Wave Tank Design

The NWT was designed to be 30 $[m]$ in length, 0.6 $[m]$ in width, and 0.72 $[m]$ in height, in x, y, and z directions respectively. The length of the wave tank is extended to 30 $[m]$ instead of 11.25 $[m]$ as in the physical experiment as an means to avoid issues with waves being reflected

from the outlet. An additional air column of height of 0.12 $[m]$ was added on top of the 0.6 $[m]$ tall wave tank to avoid execution errors in later stages. When a buoy is added after initial simulations using the original height of the wave tank, boundary errors are discovered during the simulation and the simulation was terminated automatically, reflecting error messages. The computational mesh was created with 1500 cells by 30 cells by 36 cells in the x, y, and z directions respectively. This refinement was determined after a mesh independence test was conducted (see Section 4.7). The maximum aspect ratio of the cells was maintained at close to 1 to prevent cell skewness that may eventually lead to unnecessary increase in the computational power requirement ([26]). Moreover, the disparity from high aspect ratio may lead to poor convergence during the computation due to propagation of waves, which decreases computation accuracy significantly [1]. For both simulations, a clustered mesh design was applied in the z direction so that the mesh resolution is fine at free surface and coarser at top and bottom boundaries. This was done to allow more accurate capture of the surface dynamics during the simulation while not changing the mesh designations for the whole computational domain. This improves the accuracy of the computation and surface capturing by the VOF method [32]. Figure 4.1 shows the mesh design for the simulation with the buoy included. While the mesh is clustered in the z direction, the mesh in the x and y directions is designed to be equal in cell spacing.

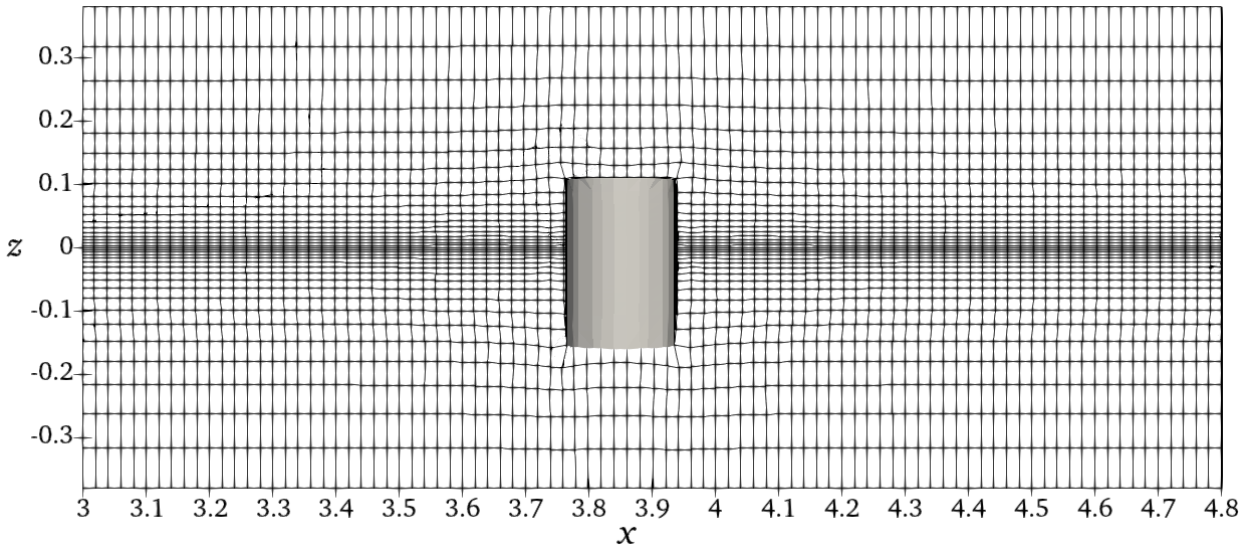

Figure 4.1: Partial clip of internal mesh for the simulation with buoy located at 3.85 [m] from the upstream edge of the NWT. The mesh in the z-direction is designed to be fine at free surface and coarse near top and bottom boundary. Some modifications are applied to shapes and sizes of cells locally for better buoy motion capturing.

The simulation time was set to 25 [s] as a longer simulation time would lead to reflected waves reaching the measurement zone, thus contaminating the data. Moreover, a longer simulation time would directly result in prolonged simulation run time. The write interval was set to be 0.1 [s] for more frequent data storage so that the time resolution of the final result is enhanced.

4.3 Floating Buoy Geometry

The simulated buoy was constrained to heave motion, to comply with conditions in the another previous physical experiment (see Appendix A). The buoy was first generated using SolidWorks CAD software and imported into OpenFOAM case folder for surface feature capturing and mesh generation in pre-processing. The submerged portion of the buoy was determined by first computing the density of the structure and then computing the submerged body volume according to the density ratio between the buoy and water. With the diameter and height of the cylinder known as 0.17 [m] and 0.26 [m] respectively, with a weight of 3.5 [kg]. The density of the cylindrical buoy was determined to be 593.07 [kg/m^3] based on the physical model. The draft measure during the

experiment (see Appendix A) was approximate, the draft for this simulation was determined using Archimedes' principle to 0.154 $[m]$ leading to a free board/air height of 0.106 $[m]$. Figure 4.2a and 4.2b shows buoy geometry from SolidWorks and the detailed alignment of the buoy within the cross section clips of internal mesh of the simulation domain in part of the measurement zone.

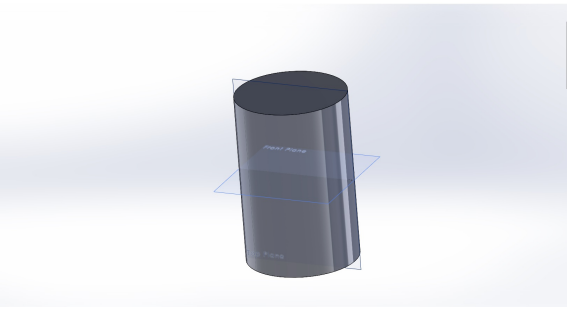

(a) SolidWorks Floating Buoy CAD

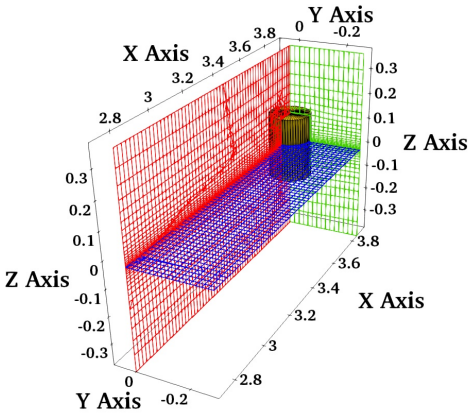

(b) The local mesh condition as well as the alignment in x, y, and z direction of the imported buoy CAD.

4.4 Temporal Discretization Settings

During the pre-processing, one of the most vital problem is the determination of the discretization scheme. The default discretization scheme for the laminar simulation of regular numerical wave tank in OpenFOAM® is the second order implicit Crank-Nicolson Method. After some test trials and analysis of the results, this scheme is changed to Euler Implicit scheme for the purpose lowering computational power requirement and maintaining stability at current selected mesh size. This is accomplished after some investigation into the Courant-Friedrich-Lewy (CFL) condition and simple observations of the surface elevation results at the simulation time required.

4.4.1 Courant-Friedrichs-Lewy Condition

In common CFD problems, the Courant-Friedrichs-Lewy condition can be used to evaluate the stability of the computation of time-varying differential equations. In detail, this condition

evaluates the the discrete rate of information update (time-step) vs the true rate of variation of a quantity. This is based on the time-step, grid size, and local velocity. Theoretically, the numerical domain for the computation must contain the physical domain [19]. The Courant number in one-dimension can be defined as shown in Equation 4.4.1 [4, 5]:

$$C = \frac{u\Delta x}{\Delta t} \tag{4.1}$$

In this equation, u represents the amplitude of velocity, with Δx and Δt being the grid size and time-step respectively. In this way, the Courant number measures the amount of information proceeds through a computational grid cell in a given time-step during the computation. To maintain the stability of the computation as well as the numerical accuracy, the Courant number should be in lower than 1. In this way, it is ensured that the information from a given cell or mesh is propagated only to the immediate neighboring cells. In generalized condition, if the Courant number is large, there are two methods to lower the value, which are increasing the grid cell size and decreasing time-step. However, many higher order discretization schemes can be stable with Courant numbers larger than 1. [19, 5].

4.4.2 The Crank-Nicolson Scheme

The Crank-Nicolson Implicit is a second order scheme in time which uses the current and previous time-step fields together with the previous time-step derivatives. This scheme is usually unstable whenever subject to complex flows around complex geometries. Stabilization is required for this scheme to succeed by off-centering the scheme by customization to mandatory coefficient in the range of [0,1] or an optional ramp function. With a coefficient of 1, the scheme is fully centered and is thus second order, while a coefficient of 0 makes the scheme almost identical to first order Euler Implicit [31].

Theoretically, the Crank-Nicolson implicit scheme is unconditionally stable, yet a low Courant

number value is still required for numerical accuracy, especially for Fluid Structure Interaction (FSI) analysis [31]. Using the Crank-Nicolson Implicit scheme, it is observed that the surface elevation record shows spurious oscillations, indicating the ratio between the given time-step as well as grid size results in a rather large Courant number ($C >> 1$). As was mentioned, the time-step should be lowered in pursue of a lower Courant number. Since the mesh independence test is already conducted, direct increase in the grid size could lead to potentials of large discretization error [21]. Therefore, the mesh size cannot be decreased since it leads to lower accuracy. As for the time-step, it needs be lowered to almost $\frac{1}{10}$ to $\frac{1}{50}$ that of previous design, which would significantly slowed down the simulation process. Therefore, the Crank-Nicolson Implicit discretization scheme is not used for the simulation.

4.4.3 The Implicit Euler Scheme

The Implicit (backward) Euler discretization scheme solves the differential equation using the current state and the next step. Comparing to Explicit (forward) Euler approach, the implicit Euler method has higher numerical stability for solving equations at large time steps [2].

As an alternative option to the Crank-Nicolson Implicit Discretization scheme, Euler implicit is applied into the simulation with the determined mesh size and time-step of 0.1 $[s]$. Comparing the accuracy of the predicted surface elevation as well as the required simulation time or computational power to previous discussed Crank-Nicolson Implicit scheme in Section 4.4.2, this scheme shows fair accuracy from a significantly faster simulation. Therefore, Euler Implicit is adopted for this simulation.

4.5 Spatial Discretization Settings

The Finite Volume Method (FVM) is used in spatial discretization for these simulations, which is a technique of discretization for partial differential equations. In the FVM, the boundaries with a

finite number of continuous Control Volumes (CVS) are defined by the numerical grids. In detail, the FVM integrates in each of these CVS, which promises the exact conservation of properties at the center of the each grid. This feature promises success in resolving discontinuity issues embedded between phases in multiphase flows. During the process of discretization, the approximations of the integrals are proceeded in the initial stage, followed by interpolation process to express the flow variables at the surfaces of the CVS regarding the values of the node [26].

In details, central difference scheme (CDS) was used to address the gradient and partially divergence, through which the Gauss' theorem is applied when transforming integrals over volume into integrals over surface. This was deemed to be effective in many situations including multiphase flow simulations ([23], [10]). As for the divergence from the phase fraction transport in Equation 2.3, the Total Variation Diminishing (TVD) difference scheme was used with van Leer limiter for conservative compression (*Gauss interfaceCompression vanLeer 1* of OpenFOAM®). Moreover, the second-order unbounded linear-upwind divergence scheme is also used for the convection terms in the momentum equation, which uses upwind interpolation weights with an explicit correction based on the cell gradient. Lastly, for the diffusion coefficient in the Laplacian terms, linear interpolation is used with the second-order unbounded *corrected* method of OpenFOAM®) regarding the surface normal gradient scheme.

4.6 Wave Absorption

Before the extended Numerical Wave Tank method to prevent reflection was selected, a clustered damping zone design was attempted for numerical wave absorption. The damping zone approach, implemented in the work of [11], and [12], involved defining part of the computational domain close to the far end of the numerical wave tank as a damping zone, in which vertical damping was applied. The surface motions were suppressed when approaching the outlet of the domain. In this design, 80% of the total cells in the x-direction were allocated to the first 50% of the geometry while the remaining 20% of the total cells were allocated to the latter 50% of the geometry with

clustered design so that the mesh was diverging in size towards the end. Figure 4.3 is an simple schematic of the clustered damping zone design and the extended wave tank design. Theoretically, the waves are damped at the end of the Numerical Wave Tank in a clustered damping zone without effects on upstream measurement zones. Theoretically, the damping should affect the surface motion only in the damping zone.

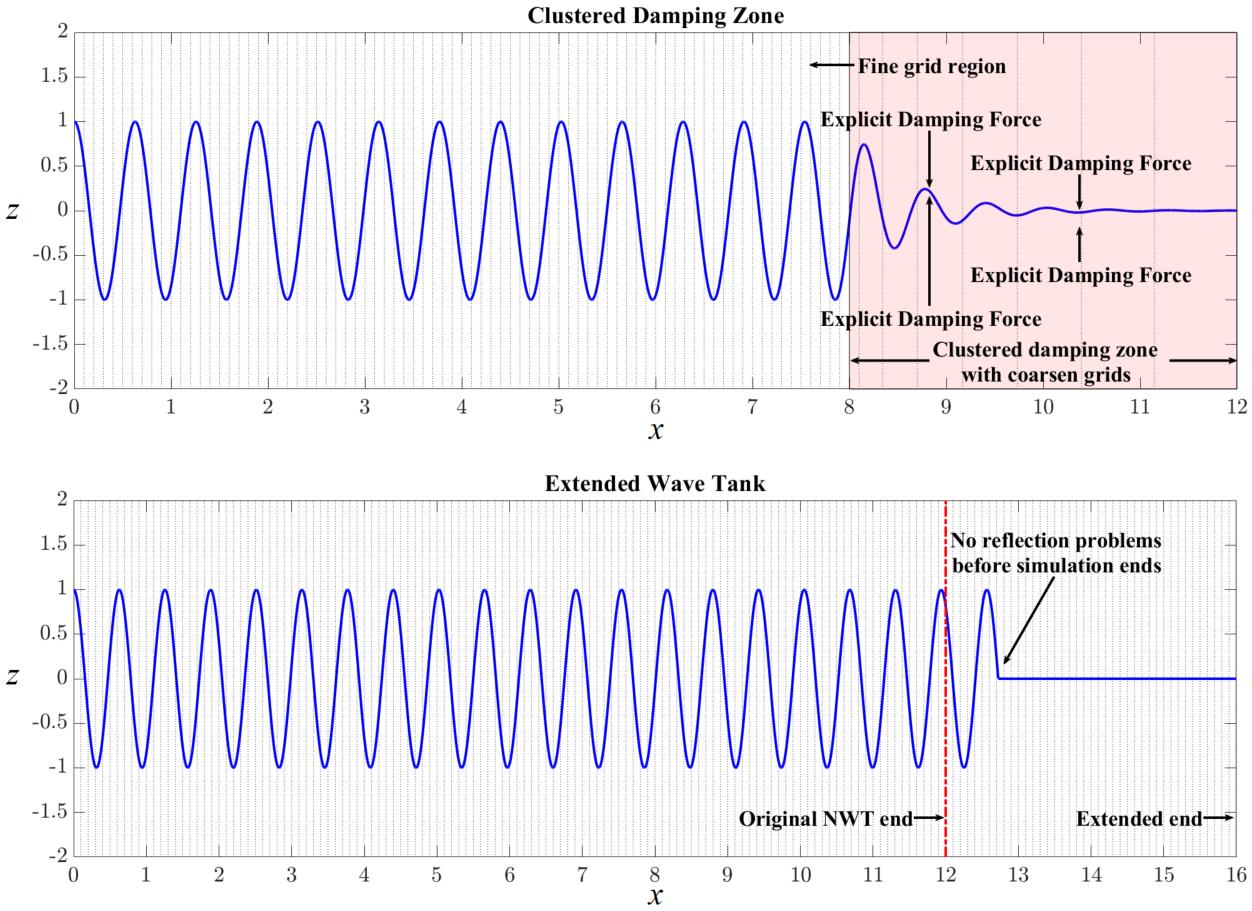

Figure 4.3: Schematic representation of the clustered damping zone design and extended wave tank design. The highlighted box (top) is the clustered coarse mesh damping zone with explicit damping force applied uniformly to the free surface, while the mesh are fine before the damping zone and no damping forces are applied to the free surface. The extended wave tank (bottom) avoids the problem of reflected wave problem for limited simulation time as reflected wave does not get to the measurement zone before simulation ends.

Figure (4.4) shows the surface elevation data from the clustered damping zone design with the heaving buoy included. The wave heights are significantly decreased from Wave Gauge 1 (WG1) to Wave Gauge 2 (WG2). Moreover, oscillating trend is discovered in Figure 4.4 where the over-

all elevation signals start to increase from some 12 [s], reaching a maximum at some 20 [s], and gradually decreasing aftermath.

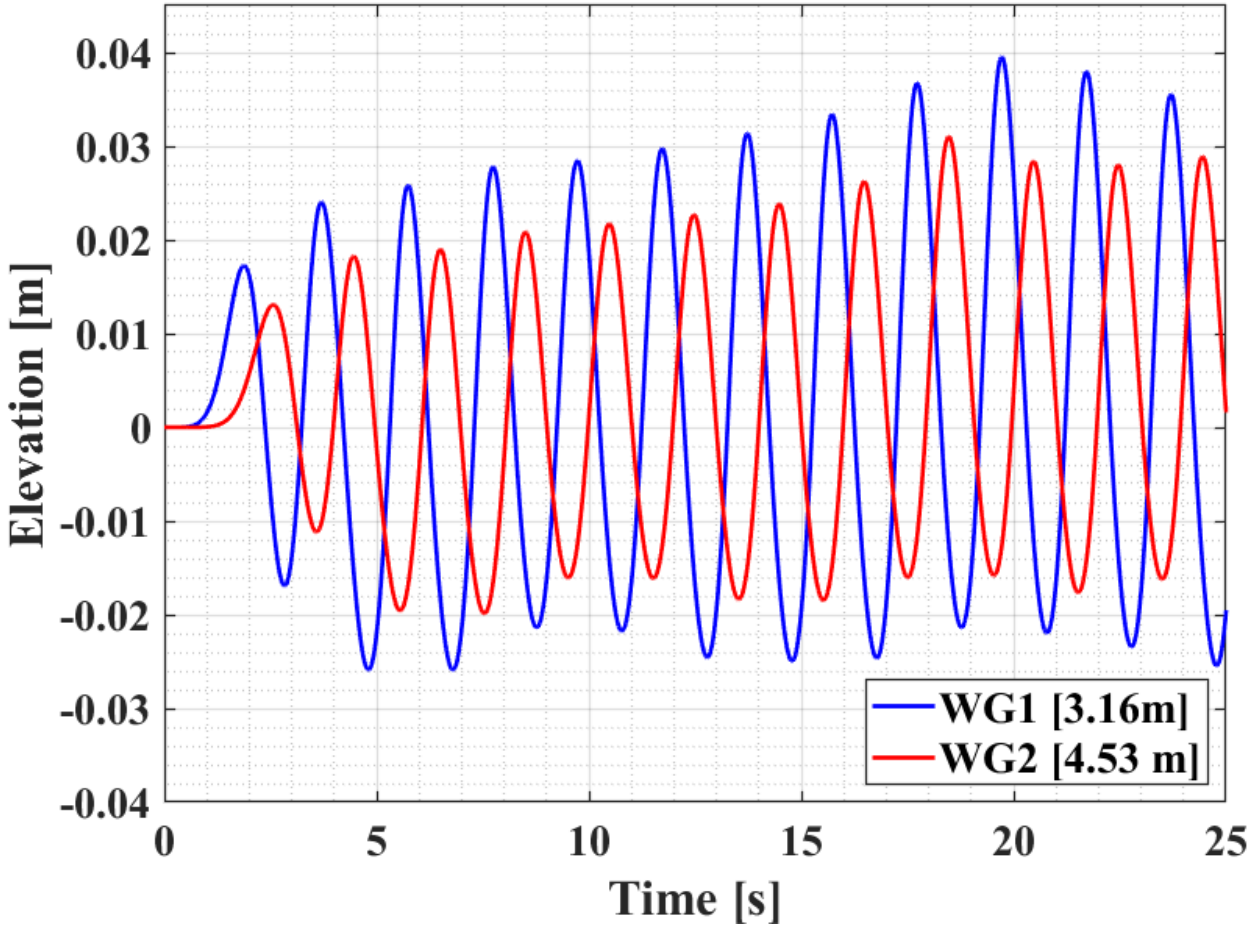

Figure 4.4: Surface elevation data from clustered damping zone design. While WG1 shows mean wave amplitude of some 0.03 [m], the wave heights for WG2 are significantly decreased (0.025 [m]).

With additional 5 measurement points along x directions, the data indicates a gradual decrease in overall signals along x direction. The mean maximum and minimum elevations from the results using this clustered damping zone technique are calculated for investigations in the decreasing trend. The results indicated dissipation problems and decay was captured by the wave gauges even if they were set to be long before the damping zone in x direction. Figure 4.5 shows the spatial

profile of mean maximum and mean minimum surface elevation from results recorded by a total of 7 wave gauges using the clustered damping zone technique.

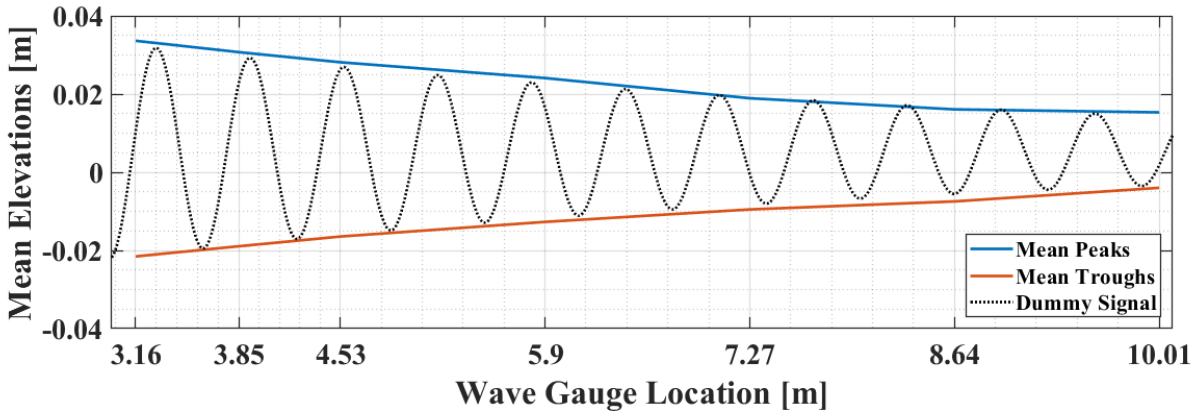

Figure 4.5: Mean maximum and minimum surface elevation in the x-direction recorded by a total of 7 wave gauges. The black dotted curve represents a dummy signal generated by an arbitrary sinusoidal function with exponential decay trend to fit the imaginary wave pattern embraced by the maximum and the minimum elevation profiles.

In Figure 4.5, the mean maximum surface elevation is decreasing and the mean minimum elevation is increasing in the x-direction, indicating decreasing wave heights along the NWT in x-direction. With the "dummy" signal generated by an arbitrary sinusoidal function with an exponential decay trend to fit the wave profile embraced by the mean maximum and mean minimum elevation signals, the dissipation for results using the clustered damping zone technique is visualized.

Multiple modifications to the design were attempted to resolve these issues including using a finer mesh, changing cluster factors, altering damping coefficient, and decreasing damping zone length. However, no apparent improvements were seen after all modifications. The clustered damping zone design was temporarily postponed as future work and the extended numerical wave tank method in Figure 4.3 was adopted in this thesis to address reflections.

4.7 Mesh Independence Tests

A mesh independence test was conducted to ensure the simulated results are not biased by the selection of mesh refinement. Theoretically, for coarse grid conditions, the discretization error will increase while too fine grid conditions tend to increase round-off errors beyond truncation, which both consequentially will lead to decreased accuracy [21]. The surface elevation from simulations based on different mesh resolutions were compared to verify convergence of the results. Table 4.1 shows the mesh options evaluated in the mesh independence test. With the previously discussed mesh option of 1500 by 30 by 36 in x, y, and z direction respectively denoted as Intermediate mesh 2, four coarse meshes, two intermediate meshes, and two fine meshes options were analyzed for mesh independence. These mesh options were chosen so that the ratio of total number of cells between two consecutive mesh options is in the range of 1.5-2.0 within intermediate mesh range.

Table 4.1: mesh independence test designations

Designations	**No. Cells** ($x \times y \times z$)
Coarse Mesh 1	250×5×6=7,500
Coarse Mesh 2	500×10×12=60,000
Coarse Mesh 3	750×15×18=202,500
Coarse Mesh 4	1000×20×24=480,000
Intermediate Mesh 1	1250×25×30=937,500
Intermediate Mesh 2	1500×30×36=1,620,000
Fine Mesh 1	1750×35×42=2,572,500
Fine Mesh 2	2000×40×48=3,840,000

The surface elevation was taken from data recorded at measurement points located at 3.16 m and 4.53 m from the upstream tank wall. Wave elevation for all mesh options above are presented

in Figures 4.6 and 4.7, respectively.

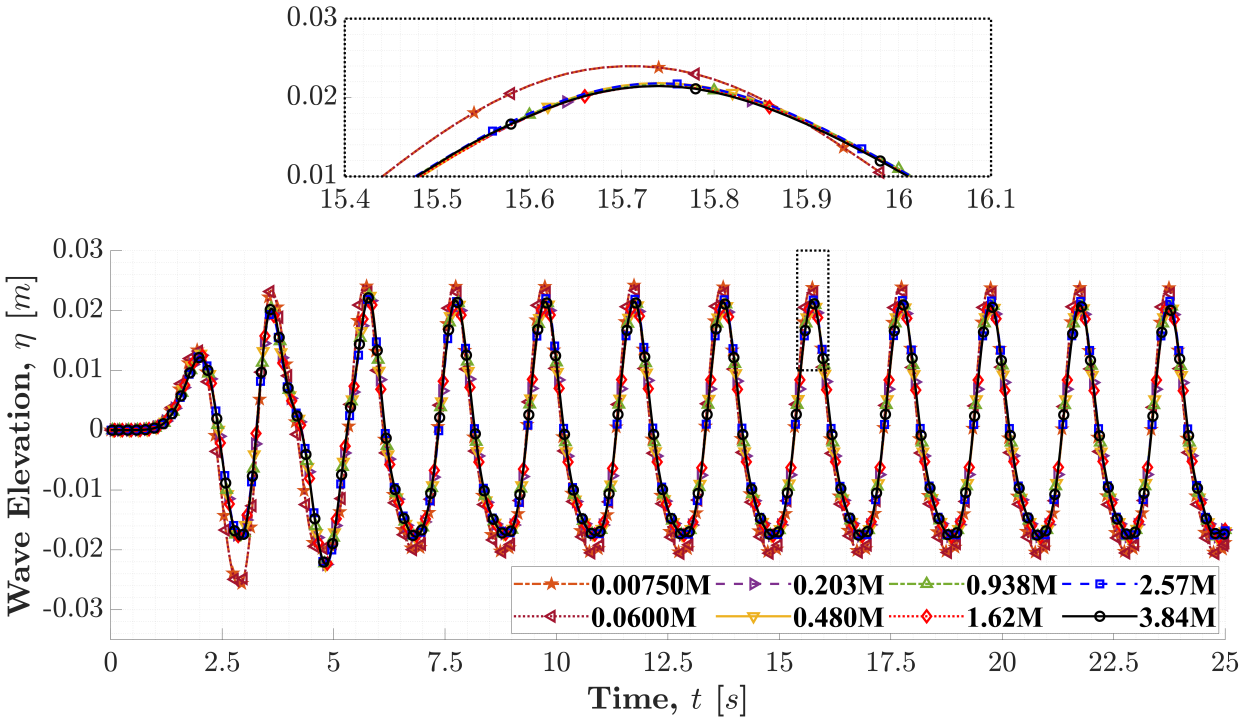

Figure 4.6: Surface elevation data from WG1 (3.16 $[m]$) reflecting convergence for the mesh independence test

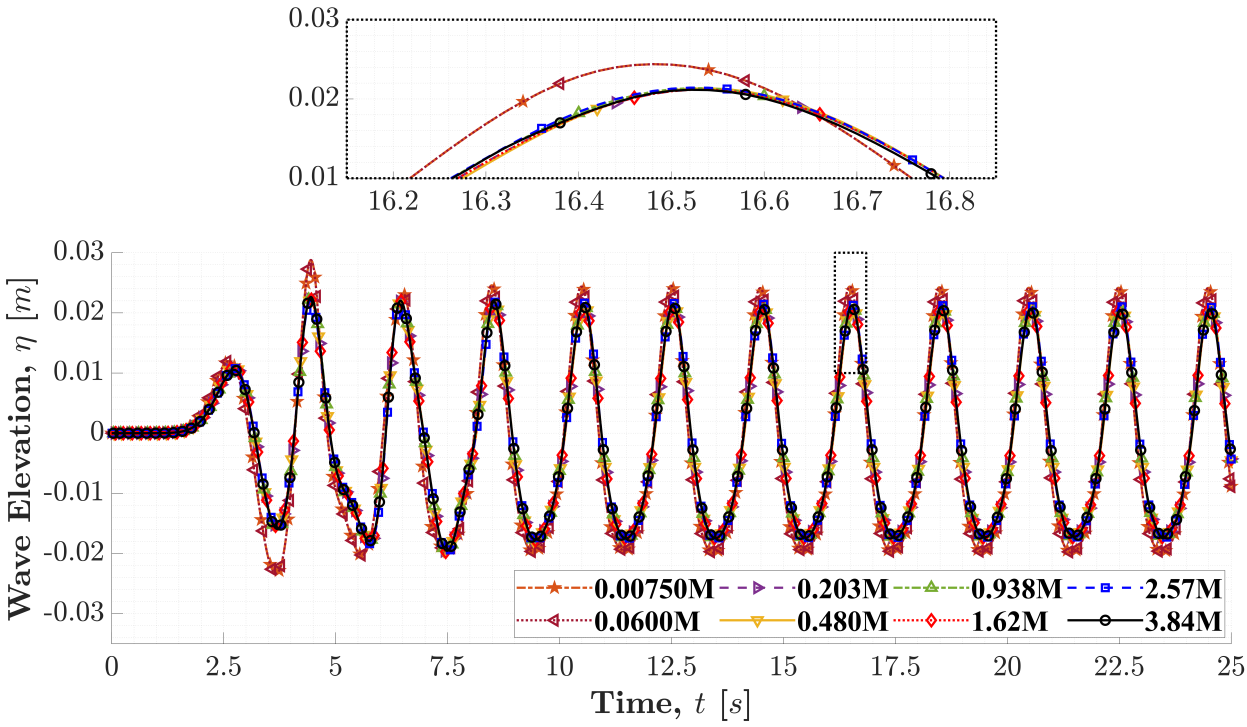

Figure 4.7: Surface elevation data from WG2 (4.53 $[m]$) reflecting convergence for the mesh independence test

Magnified plots for the selected peaks (dashed box) are presented to show detailed differences between the different meshes in Figure 4.6 and 4.7. As seen in the magnified box in both plots (Figure 4.6 and 4.7), the elevation data appears to be converging except for a significantly higher peak discovered for the most coarse mesh in Figure 4.6 and 4.7. Moreover, unexpected small changes in the wave shape is discovered at some 4.2 $[s]$ for WG1 and 5.3 $[s]$ for WG2. Although the cause of this problem is not well understood, this change in the trajectory is suspected to be transient behavior since the problem occurs at early stage during the propagation and no recurrence is discovered at later times. Since this is consistent for all mesh refinements, the simulation passes the independence test.

Detailed mean peak and trough amplitudes for each mesh option were also computed. Due to the consideration of waves being not fully formed at the beginning of the simulation, the first peak value of the signals from both WG1 and WG2 were excluded in the mean peak amplitude

calculation. The results are presented in Figure 4.8.

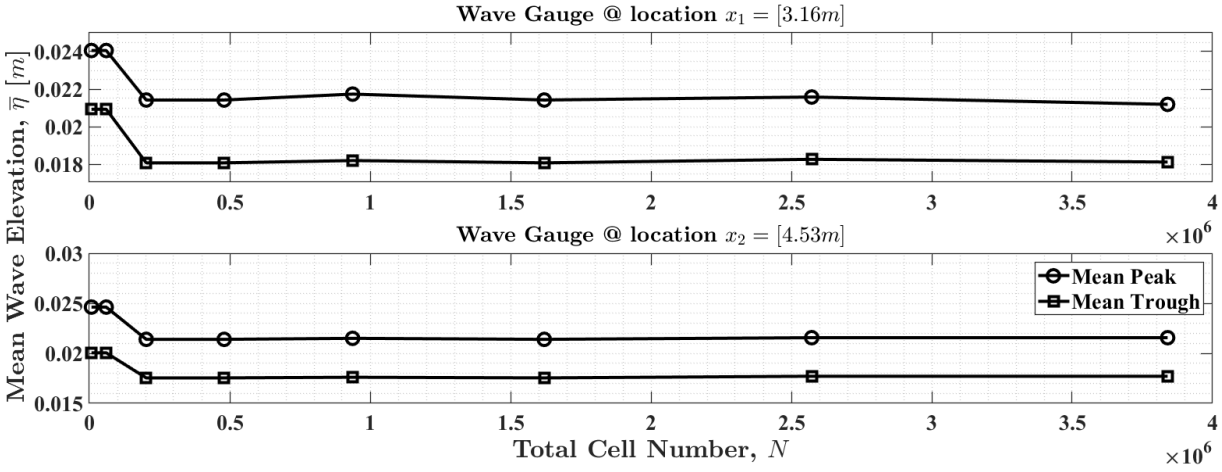

Figure 4.8: Mean peak and trough amplitude at WG1 (3.16 m) and WG2 (4.53 m)

For both wave gauge locations, the mean peak and trough amplitude difference remain almost unchanged between different mesh designations except for the Coarse Mesh 1 where a significant increased wave elevation was discovered. The mean peak amplitude was 0.0214 [m] for Intermediate Mesh 2 (the one used for further simulation) at both wave gauge locations. The mean trough amplitude was 0.0181 [m] for WG1 and 0.0176 [m] for WG2. The percentage difference in mean peak and trough amplitudes between other meshes and the Intermediate Mesh 2 were computed and presented in Tables 4.2 and 4.3.

Table 4.2: percentage difference in mean peak amplitude with respect to the Intermediate Mesh 2

Mesh	WG1 Difference	WG2 Difference
Coarse Mesh 1	12.6%	15.0%
Coarse Mesh 2	12.6%	15.0%
Coarse Mesh 3	1.40%	1.40%
Coarse Mesh 4	1.40%	0.935%
Intermediate Mesh 1	0.935%	0.935%
Fine Mesh 1	0.935%	0.935%
Fine Mesh 2	0.935%	0.467%

Table 4.3: percentage difference in mean trough amplitude with respect to the Intermediate Mesh 2

Mesh	WG1 Difference	WG2 Difference
Coarse Mesh 1	15.5%	14.3%
Coarse Mesh 2	15.5%	14.3%
Coarse Mesh 3	1.14%	1.42%
Coarse Mesh 4	0.552%	0.935%
Intermediate Mesh 1	0.552%	0.571%
Fine Mesh 1	0.552%	0
Fine Mesh 2	0	0

The percentage difference indicates significantly higher error for Coarse Mesh 1 and Coarse Mesh 2. The overall percentage difference between the selected mesh and most other meshes were below 1%, some percentage differences higher than 1% was discovered for coarse mesh designations. These differences were nevertheless very close to 1% so that the error is deemed to be

acceptable.

5. RESULTS AND DISCUSSIONS

After the simulations finished, the first attempt in direct visualizing the results are evaluating the animations of the simulation by using the ParaView application. In this step, the computation results at each time-step are combined together and visualized frame by frame, for which the final production is an animation of the simulated motion of fluid. In addition, the case can be reconstructed over a certain time interval after the decomposition for parallel processing. The significance of such reconstruction lies in the accessibility to the surface features analysis. Other options of post-processing include the recorded surface elevation data as well as the dynamical response of the heaving buoy during the simulation at the assigned measurement zone.

5.1 Time Series of Waves

The surface elevation data is presented here as time series of wave elevation. Figure 5.1 shows the visualized surface elevation data for both WG1 (in blue) and WG2 (in red). The mean peak amplitudes are 0.0214 $[m]$ for both WG1 and WG2. The mean trough amplitude is 0.0181 $[m]$ for WG1 and 0.0177 $[m]$ for WG2, the wave heights are 0.0395 $[m]$ at WG1 and 0.0391 $[m]$ at WG2. Unexpected small changes in the wave shapes are also discovered in Figure 5.1 at some 4.2 $[s]$ for WG1 and 5.3$[s]$ for WG2. The cause of this is suspected to be transient behaviors as was explained in Section 4.7 and shown in Figure 4.6 and 4.7.

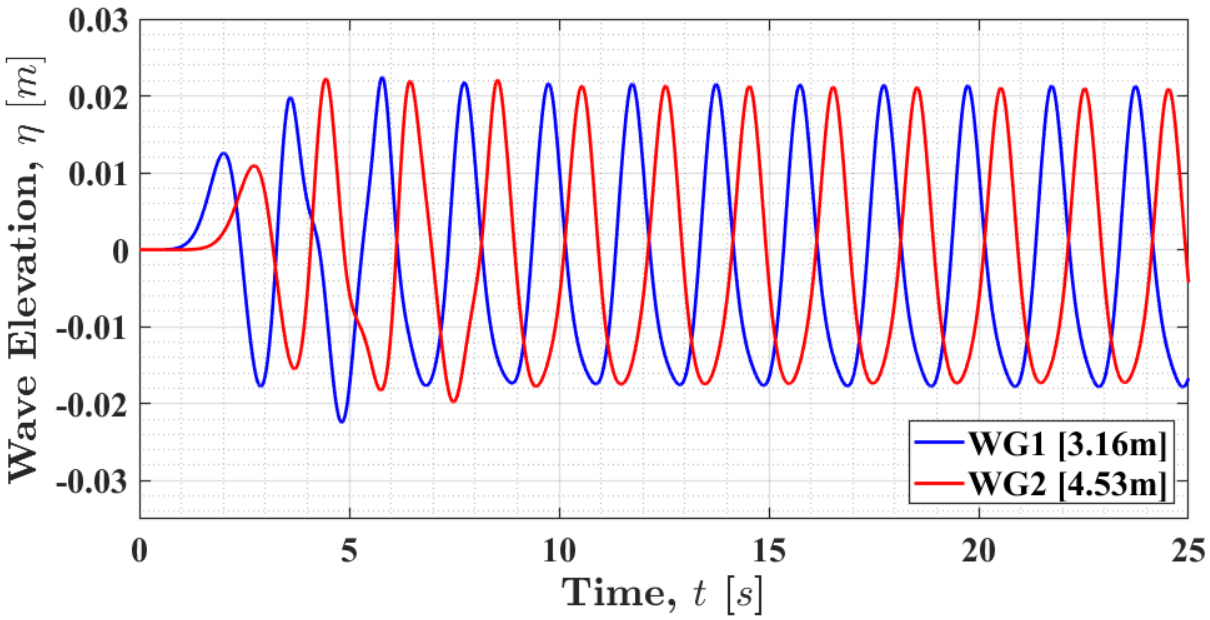

Figure 5.1: Surface elevation from WG1 and WG2 after simulation without buoy involvement.

5.1.1 Experimental Data Processing: Correlation and Savizky-Golay Filtration

Before the data from the physical experiments are used in comparison to the numerical results, some data processing are done to enhance the signals from the experiment. There are two major problems in the experimental data.

Firstly, the wave gauges used in the experiment directly recorded the voltage signals instead of surface elevation, for which a small difference is expected. In order to overcome this issue that may lead to falsely and meaningless validations, the wave gauges are calibrated at the beginning of the physical experiment. The wave gauges are manually set to several pre-decided heights and compared to the signals received from the wave gauge. With multiple trials of different heights, a linear regression relationship is established to translate the voltage data into surface elevation.

Secondly, the experimental data yet contains too much noise from vibrations during the experiment that even after calibration are finished. The Savitzky-Golay data smoothing technique is

applied to the surface elevation data after correlation for noise cancellation. The Savitzky-Golay filtering is a low-pass technique shown to have desirable properties in time-domain data smoothing. When the signals are shown to be slowly varying in the temporal span while corrupted by local random noise, the Savitzky-Golay filter allows replacement of data with polynomial convolutions with surrounding data points. The significance of this action lies in that the obtained value is not biased while the noise can be reduced due to nearby data points sharing almost the same underlying values in any slowly varying trend [25].

There are two parameters for the Savitzky-Golay data smoothing, the order of polynomial convolution applied to the signal and the frame length within which the convolution occurs. However, no concrete source of information on designations of these two parameters were found and the parameters are determined only from trial and error. Figure 5.2 shows the details of this data smoothing technique using the control experiment signal. As is shown in Figure 5.2, the smoothing technique is capable of canceling noise for the measured elevation signal while not distorting the underlying signal.

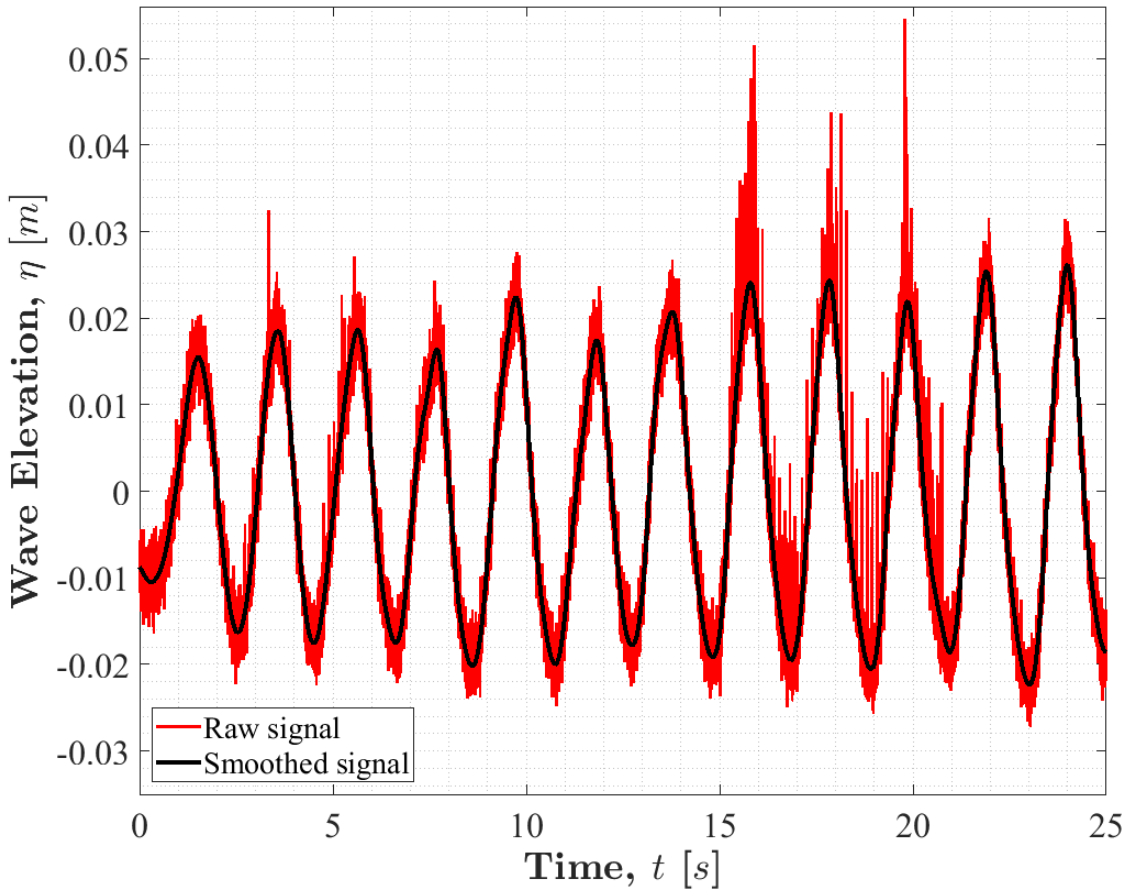

Figure 5.2: Time Series of Wave Elevations: Raw signal (red) and smoothed signal (black) using the Savitzky-Golay data smoothing technique. The frame length and order of convolution is determined to be 501 and 3 respectively.

5.1.2 Surface Elevation Results Validation

In order to validate the simulation results of the wave field, the surface elevation from WG1 is compared to the control experiment, where no buoy was involved, see Figure 5.3. The experimental results are first smoothed with Savitzky-Golay filtration for noise cancellation, then phase shifted to skip the relatively flat initial stage. In Figure 5.3, it is shown that the numerical results matches fairly well to the experimental data in general. Some initial mismatch can be seen, which can be the result of transient behaviors. In addition, a small disparity in wave frequency is discovered. This could be due to the fact that the wave maker of the physical wave tank was controlled by an analog dial, from which a small frequency error can be expected. The mean peak and trough

amplitude of the experimental results were calculated, and compared to the ones from the numerical simulation. The percentage difference between numerical results and experimental results are calculated and presented in Table 5.1.

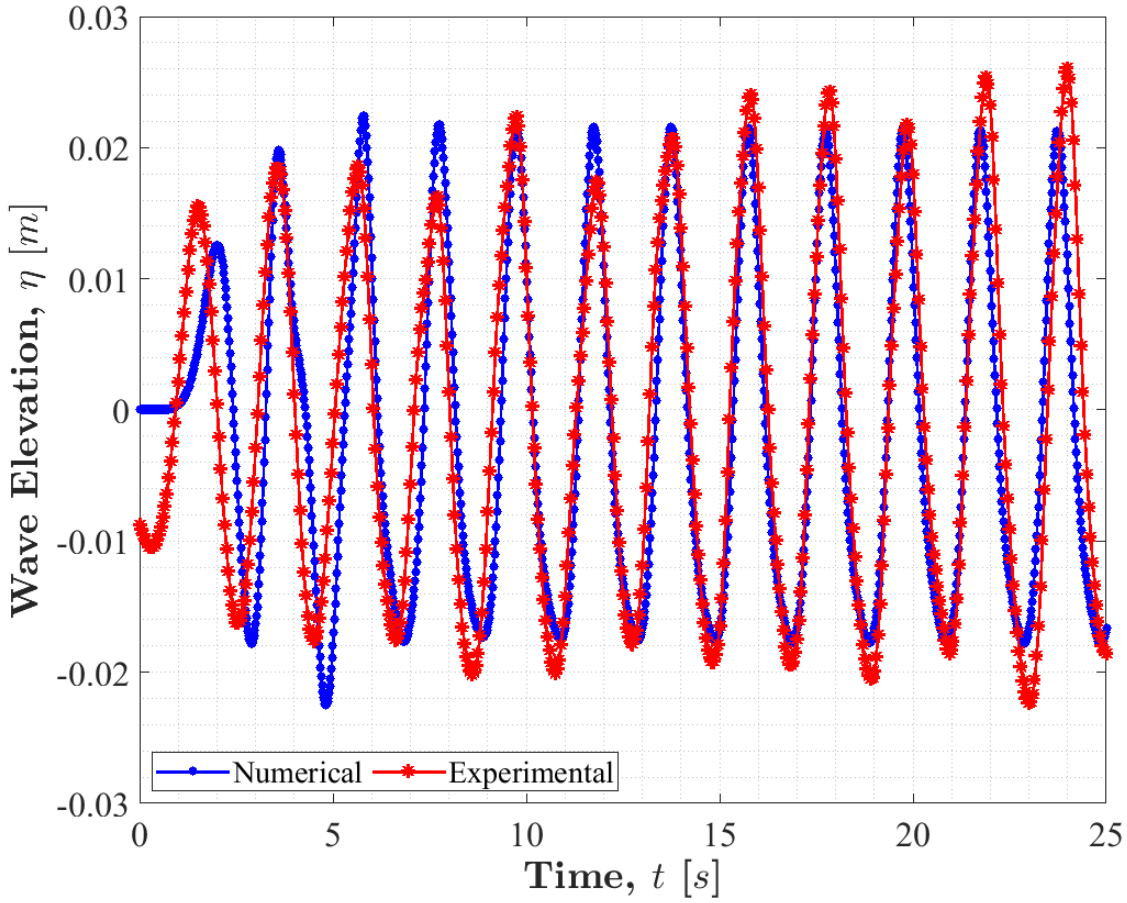

Figure 5.3: Surface elevation from WG1 plotted with the experimental data after processing.

Table 5.1: numerical results in comparison to experimental for free wave propagation.

Results	**Mean peak [m]**	**Mean trough [m]**
Numerical	0.021	0.018
Experimental	0.021	0.019
% Difference	0	5.3%

Similar to the calculation of mean peak and trough amplitude in the mesh independence test, the first peaks from both simulation signals and experimental signals were excluded in these calculations. From Table 5.1, a 5.3% relative error is discovered in mean trough amplitude together with good agreement in mean peak amplitudes at 0.021 [m]. By simple addition of the mean peak and mean trough amplitudes, the mean wave height is 0.039 [m] for the numerical simulation and 0.040 [m] for the experimental data, which amounts to a 2.5% difference.

5.2 Heave Motions of the Floating Buoy Measurements

Previous existing experimental results [30] has been used for further evaluation. For details of their experimental set up, see Appendix A. The coordinates of the cylinder centroid, together with the translational velocity in z-direction, were extracted from the simulations featuring the floating buoy. These was used to analyze the buoy motions. The heave profile were compared to the results from Appendix A for validation. Figure 5.4 shows the heave motions as well as the translational velocity in z-direction of the floating buoy from the laminar simulation. The signals are truncated to present only results from 11.67 [s] to 25 [s] to skip the transient behaviors. As is shown in Figure 5.4, the heave profile from Laminar simulation features sharper and higher maximum heave peaks and rather alleviate minimum heave. This matches the nonlinear behaviors in the description of Second-order Stokes waves.

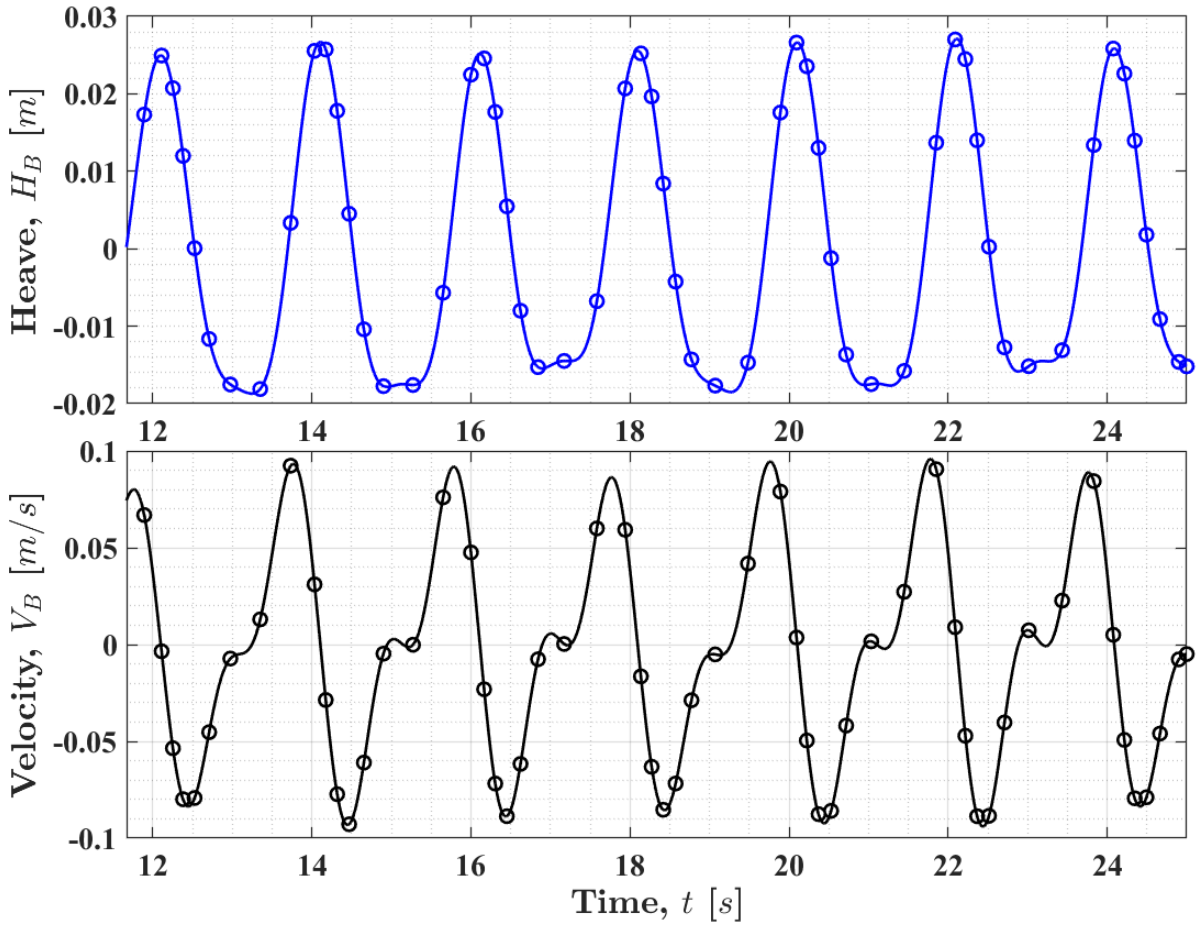

Figure 5.4: Heave and translational velocity in z-direction profile of the floating buoy from Laminar simulation

Utilizing both top plot (heave) and bottom plot(velocity) of Figure 5.4, some relationships between the heave and translational velocity in z-direction is discovered. Firstly, the profile of translational velocity in z-direction shows a secondary small peak between each pair of maximum and minimum velocities. The occurrence of this behavior coincide the time when the buoy is at minimum heave. This is also due to the nonlinear behavior of the Second-Order Stokes wave. Secondly, the maximum and minimum velocities both take place when the floating buoy is at free surface (H_B = 0). However, the maximum velocity takes place when the buoy is at free surface yet trending to reach maximum heave. On the contrary, the minimum velocity takes place when the buoy is at free surface yet trending to reach minimum heave. Thirdly, when the buoy is at

maximum heave and minimum heave, the translational velocity of the buoy is zero.

5.2.1 Heave results Validation

The heave profile from the laminar simulation is compared to the results from Experiment (s) for validation in Figure 5.5.

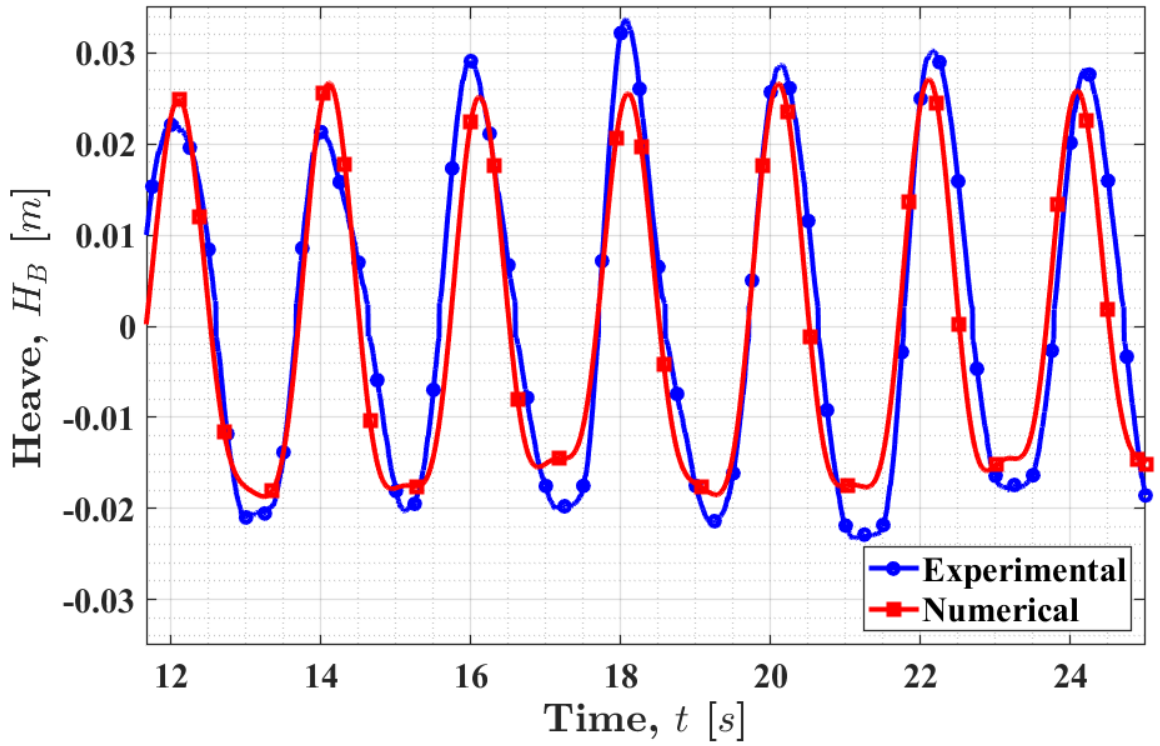

Figure 5.5: Comparison of Heave motion from the Laminar simulation and the results from Experiment (2)

The trajectory of the heave from laminar simulation matches that of Experiment 2 (details in Appendix A) [30]. However, some over-estimation of minimum heave and under-estimations of the maximum heave are discovered from the comparison, especially after some 16 $[s]$. The mean maximum and mean minimum heave motion of the experimental results are computed by first computing for data obtained by three different measurement techniques (Accelerometer, Visual Simultaneous Localization and Mapping (VSLAM) algorithm, and Kanade-Lucas-Tomasi (KLT)

algorithm) then calculating the mean of these three mean values. In this way, the mean of the maximum and minimum heave motion from the experiment is computed as 0.028 $[m]$ and 0.022 $[m]$ respectively. The mean magnitude of maximum and minimum heave from the laminar simulation is also computed and compared to the results from Experiment 2 for more in-depth investigation of the accuracy level. The comparison is shown in Table 5.2.

Table 5.2: Difference in mean maximum and minimum heave motion compared to experimental results.

Simulation Approach	**Max Heave $[m]$ and % Difference**	**Min Heave $[m]$ and % Difference**
Laminar	0.026 (7.14%)	0.017 (22.7%)

The maximum heave from laminar simulation indicated a low percentage difference from that of Experiment 2 at some 7%. However, a large percentage difference at some 23% is seen for the mean minimum heave comparison. This is due to some numerical errors in the simulation. The motion of the buoy is allowed in the laminar simulation with the movement of mesh. This will lead to increased cell skewness for the region above and below the floating buoy against the boundaries when the buoy is at maximum and minimum heave location respectively, which will lead to inaccuracy in simulations.

5.3 Force Measurements

The forces exerted on the buoy by incident waves were measured during the simulation. Similarly, the signals are truncated to present only from 11.67 $[s]$ to 25 $[s]$ in avoidance of the initial transient behaviors. The pressure force and viscous force in the y-direction are trivial due to symmetry. Figures 5.6 and 5.7 shows the profiles of pressure force and viscous force respectively in both x- and z-directions.

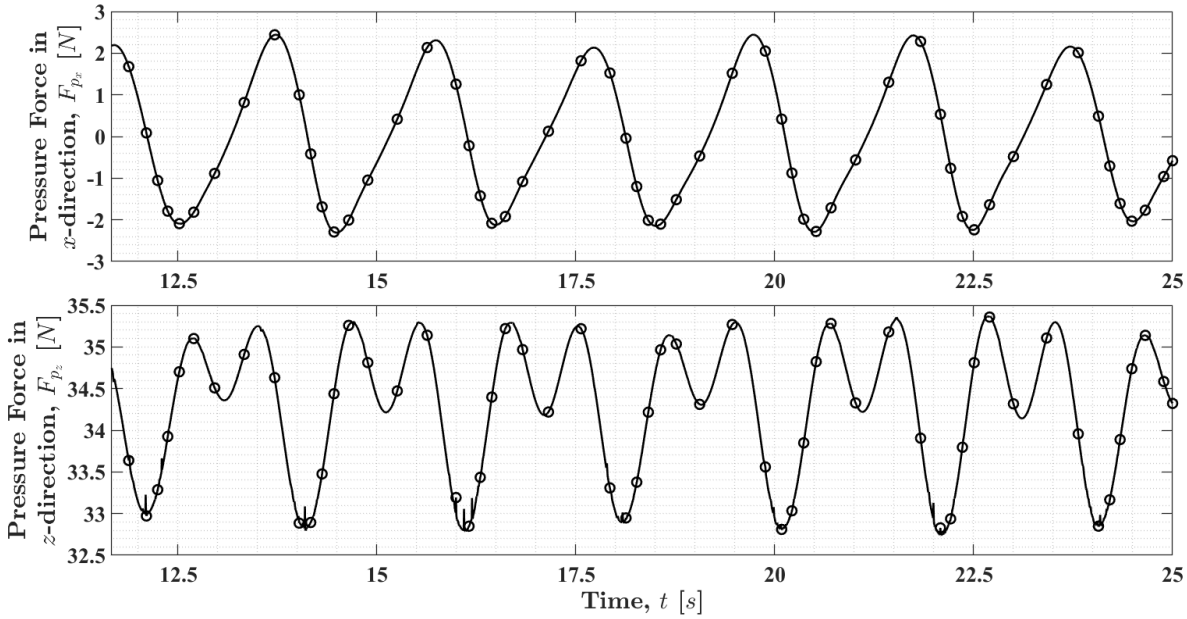

Figure 5.6: Profile of pressure forces exerted on the buoy in the x- and z-directions due to incoming waves.

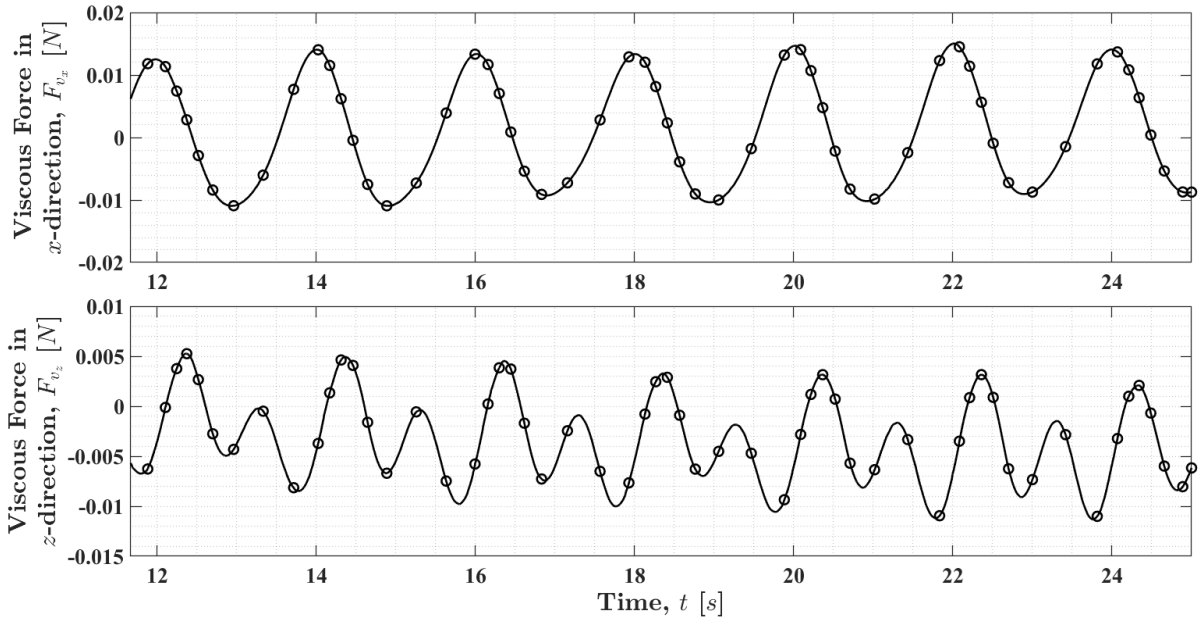

Figure 5.7: Profile of viscous forces exerted on the buoy in the x- and z-directions due to incoming waves.

Comparing the the magnitude of pressure forces and viscous forces in Figure 5.6 and 5.7, the

pressure force in z-direction shows dominating effect on the buoy with much larger magnitude than the viscous forces and even pressure force in x direction. This is expected since the buoy was constrained to heave motion only during the simulation. Some data jumps are discovered at minimum pressure force in z-direction in Figure 5.6. This is due to the same numerical error caused by increased cell skewness when buoy is at maximum and minimum heave, mentioned in Section 5.2.1.

The lift force and drag force were computed in the z- and x- directions respectively by summation of pressure forces and viscous forces at each time step in the z- and x- directions respectively, see Figure 5.8. Similarly to the pressure force and viscous force profile, the data for lift and drag forces were also truncated to cover the same time frame in resolving transient behaviors.

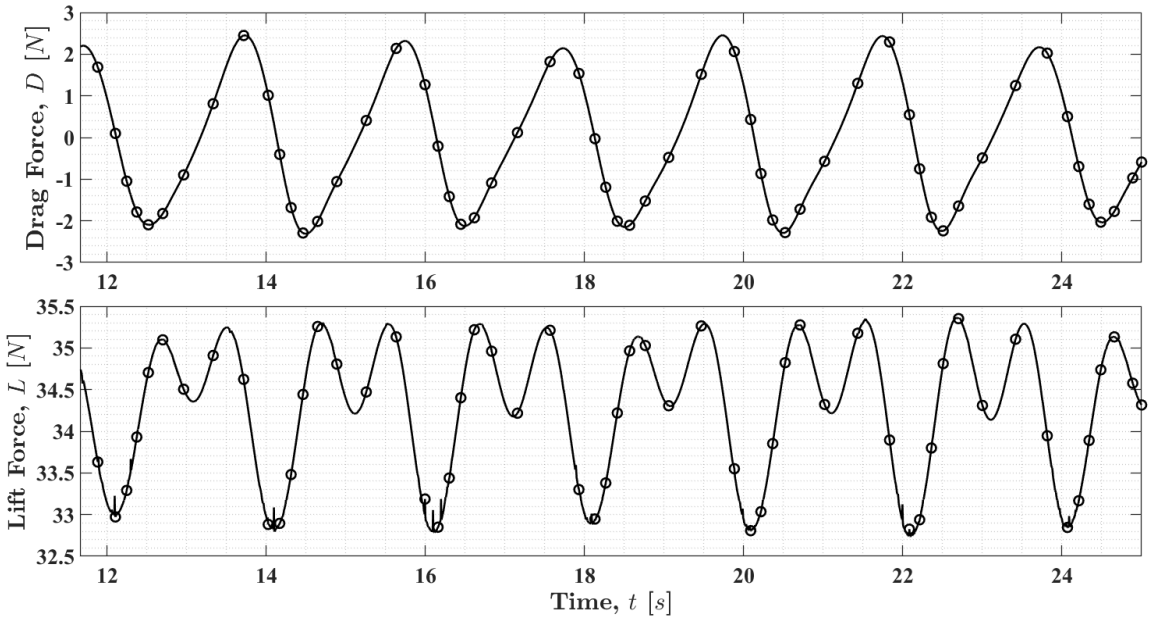

Figure 5.8: Lift and drag force times series on the buoy due to incident waves.

As was discussed in Section 5.3, there is a dominating effect from pressure force in z-direction. Since the lift force is the summation of the dominating pressure forces and small scale viscous

forces in z-direction, the similarities in trajectories and magnitude between Figure 5.8 and Figure 5.6 is expected. Similarly, the issue of jumps of data at minimum lift force is discovered due to the same numerical error of increased cell skewness.

5.4 Numerical Error Correction

As was previously discussed in Section 5.3, numerical errors of small data jumps were discovered in Figure 5.6 and 5.8 for minimum pressure force in z-direction and minimum lift force. Even if the mesh independence analysis was conducted and proven to converge for the selected mesh designation, no additional mesh independence analysis was conducted for the simulation with the buoy added. The heave of simulated buoy was facilitated by dynamical mesh point displacement during the simulation which will increase the cell skewness for areas above and beneath the buoy when the buoy is at peak and trough, respectively. In order to resolve the increased skewness of the areas above and beneath the buoy, mesh refinement to increase mesh size and increasing inner dynamical mesh region was attempted. The significance in this technique lies in fixing numerical errors by improving mesh resolutions while not changing the mesh designation for the whole computational domain. However, this lead to overwhelming computational power demand and the simulation time is increased significantly. In details, 17 hours are required to finish this 2-phase simulations without turbulence considerations, which is almost 4 times in simulation time comparing to previous design. Moreover, decreased wave heights and unexpected oscillations are discovered when mesh refinement is applied to the measurement zone in the time series of wave series. In this way, the mesh refinement technique is not used in this research despite the compelling advantages.

Similarly to the raw experimental signal, these error can be treated as random noise and smoothed by the Savitzky-Golay filtering technique in 5.1.1. Since only small region of noises are witnessed in both time series of pressure force and lift force, the frame length and the order of convolution are chosen to be 40 and 2 respectively. Figures 5.9 shows the smoothed signals using

Savitzky-Golay filtering techniques.

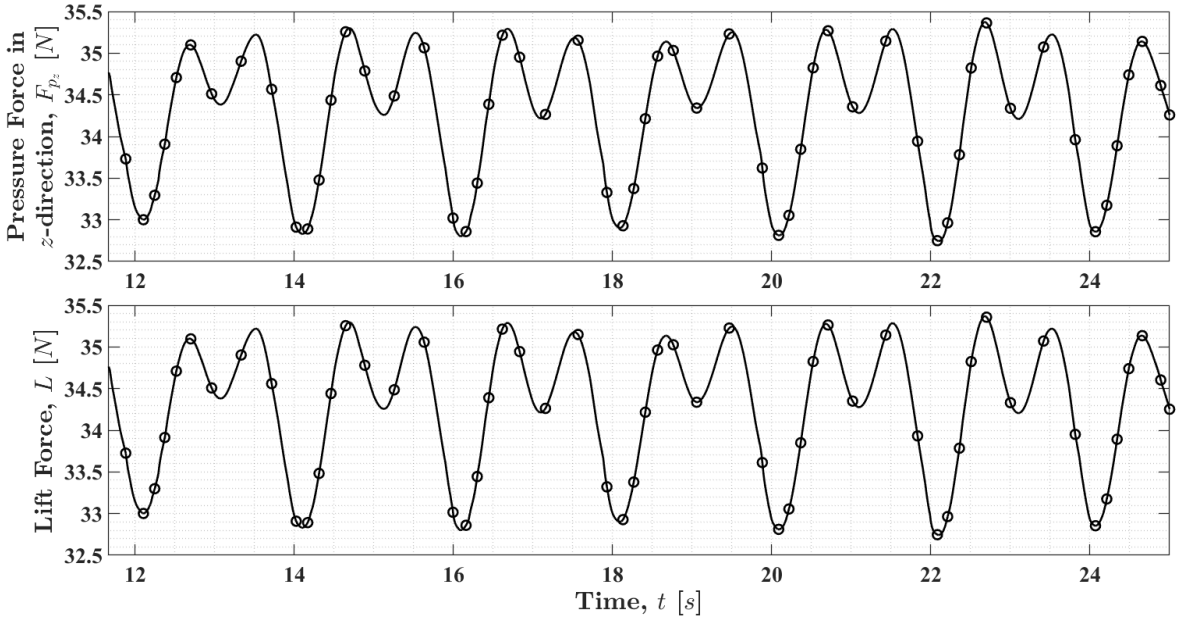

Figure 5.9: Profile of pressure forces in z-direction and lift force exerted on the buoy due to incoming waves, with Savitzky-Golay smoothing method applied. Frame length is 40 and the order of convolution is 2

As is shown in both plots in Figure 5.9, the small jumps of data in results from laminar simulation presented in FIgure 5.6 and 5.8 are resolved by the smoothing process and the general trend and magnitude of signals are not changed comparing to 5.6 and 5.8. In addition, the mean lift force exerted on the floating buoy was recalculated after the Savitzky-Golay smoothing is applied to the signal and the results indicates identical value of 34.18 $[N]$.

However, the mechanism behind the application of the Savitzky-Golay filtering techniques is yet not well understood in terms of determinations of both frame length and order of convolution [25]. Moreover, the application of data smoothing in the field of numerical modeling remains controversial since many researchers in the field of numerical modeling yet consider this mechanism to be an act of data manipulation, especially for most parametric modeling [25]. In this way, further investigations into the mechanisms of such data smoothing techniques regarding frame length

and the order of convolution is required for more concrete judgement.

5.5 Scheme-to-scheme Comparison

The same 2-phase incompressible flow problem with floating buoy constrained to heave motion only in this research is replicated using Reynolds Averaged Navier-Stokes (RANS) scheme and Partially Averaged Navier-Stokes (PANS) scheme by [13]. The results are used for comparison with the laminar results from this research in terms of accuracy level and computational power cost (simulation execution time).

5.5.1 Heave Comparison

Figure 5.10 shows the heave and velocity profiles of the buoy. The same truncation of signals was conducted to compare data from 11.67 [s] to 25 [s] only while avoiding the initial transient behaviors.

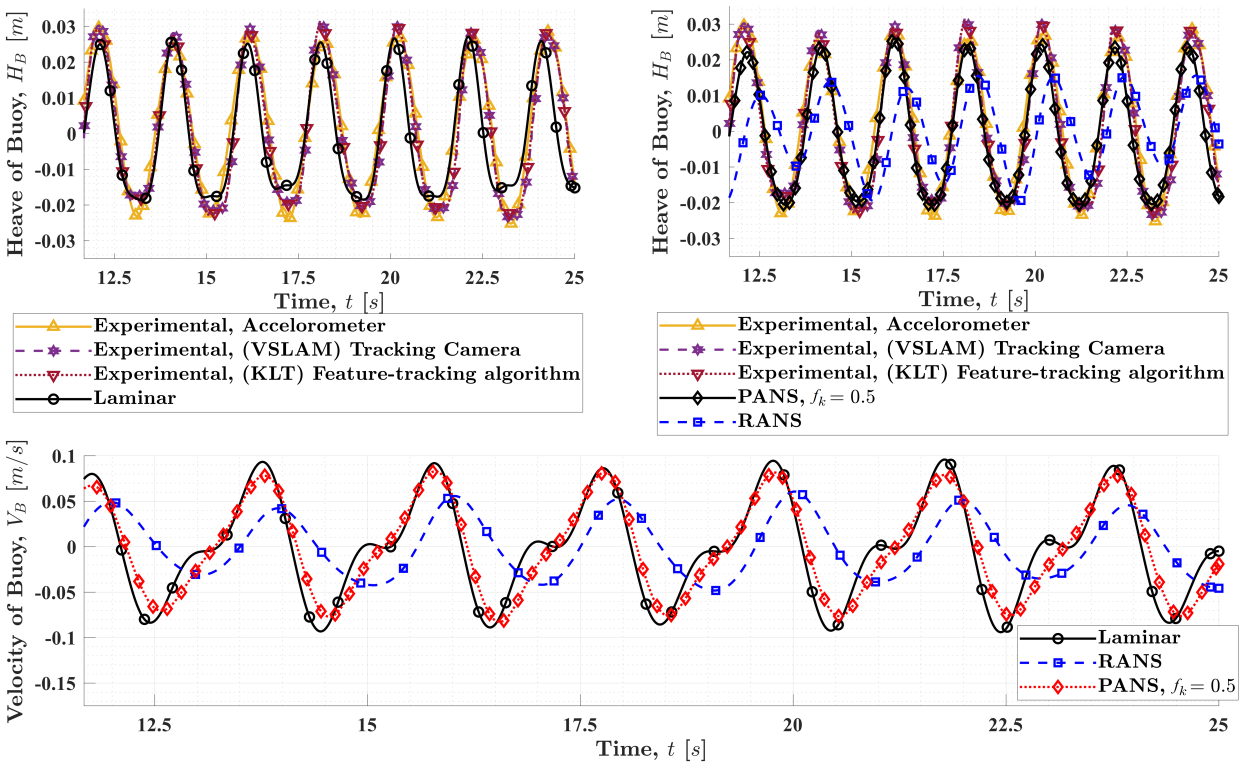

Figure 5.10: Time series of buoy heave and velocity profiles.

The heave profile from laminar and PANS simulations match fairly well with the experimental data while RANS simulations show under estimated heave motions and shows different trajectories. Both laminar and PANS simulation show a flat minimum heave, which is also seen in the experimental data. The reason for this is due to the heave motions being subjected to the nonlinear second-order Stokes wave as discussed in Section 5.2. This is also implicitly indicated in the velocity profile by a secondary peak in the laminar results and a left-skewing trend in the PANS results. The mean of the maximum and minimum heave motions are also computed for RANS and PANS simulation. Together with the mean of maximum and minimum heave of laminar simulation computed in 5.2.1, these mean values are compared with the experimental results for validation. The comparison is shown in Table 5.3.

Table 5.3: difference in mean maximum and minimum heave motion compared to experimental results. The mean heave from all three measurement techniques in the experiment were used as the reference in the percentage analysis.

Simulation Approach	**Max Heave [m] and % difference**	**Min Heave [m] and % Difference**
Laminar	0.026 (7.14%)	0.017 (22.7%)
RANS	0.014 (50%)	0.014 (36.4%)
PANS, $f_k = 0.5$	0.024 (14.3%)	0.020 (9.09%)

As is shown in Table 5.3, the relative error between RANS simulation heave data and experimental data is very high (50% for mean of maximum heave and 36% for mean minimum heave). As for PANS, the comparison unveiled small (9%) percentage difference in mean minimum heave and some 14% percentage difference for mean maximum heave. In this way, the PANS scheme showed satisfying accuracy regarding the prediction of heave motion.

5.5.2 Force Comparisons

Due to no experimental results of force measurement during the experiment, the force data from the simulation are not validated with experiments. Instead, with PANS results showing overall acceptable accuracy in the prediction of heave motion when compared to the results from Experiment 2 (see Section 5.5.1), the force data from the PANS simulation is used as a reference for comparison of force profiles recorded during both laminar simulation and RANS simulation.

Figures 5.11 and 5.12 show respectively the pressure force and viscous force profiles from laminar, RANS, and PANS simulations in $[N]$. The upper plots in both Figures 5.11 and 5.12 display force profiles in x-direction with the lower plot being force profiles in z-direction.

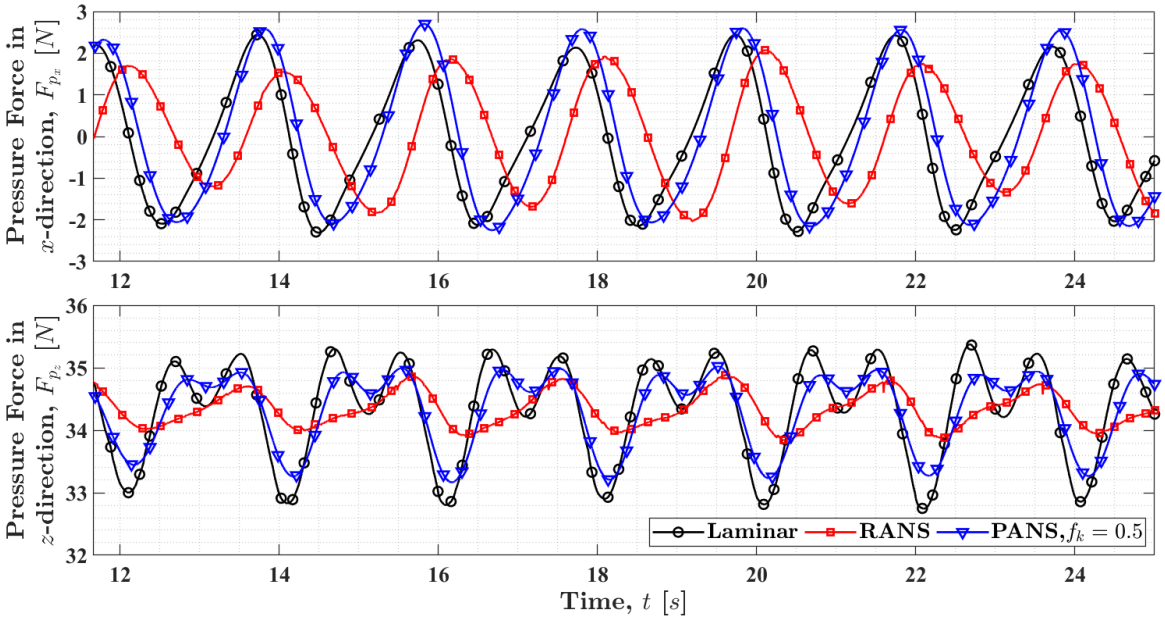

Figure 5.11: Profile of pressure forces exerted on the buoy in the x- and z-directions due to incoming waves from laminar, RANS, and PANS simulations

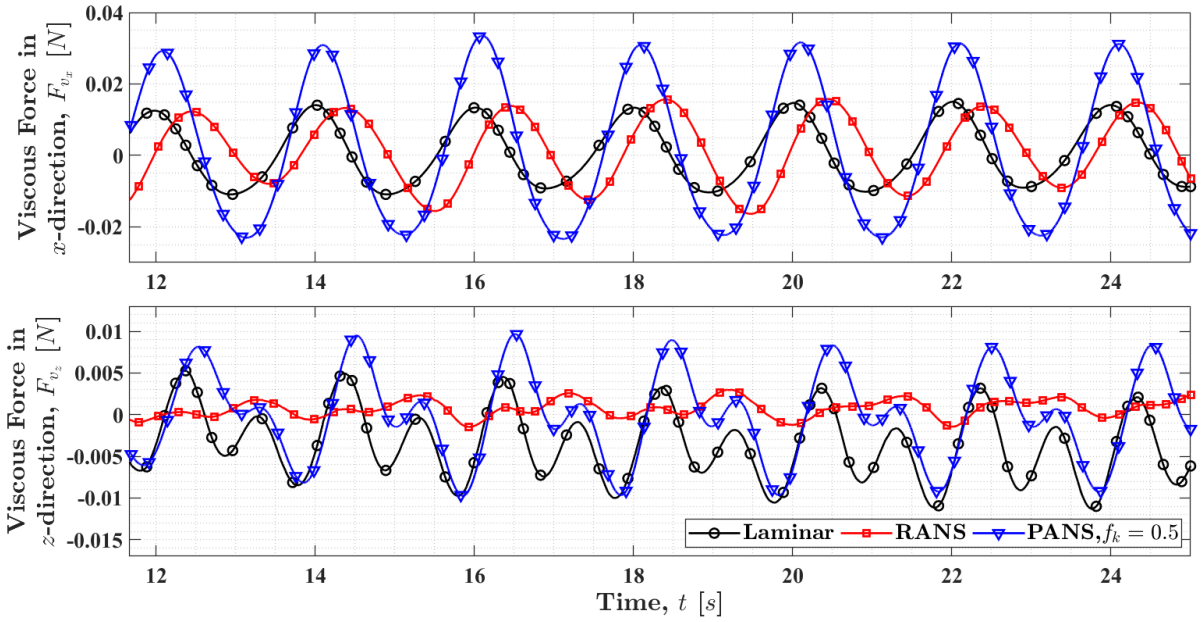

Figure 5.12: Profile of viscous forces exerted on the buoy in the x- and z-directions due to incoming waves from laminar, RANS, and PANS simulations

The RANS simulation estimated lower pressure force change in x-direction and totally different trajectory and magnitude for pressure force in z-direction in Figure 5.11 comparing the results from laminar simulation and PANS simulation. Moreover, a slight shift of the signal is discovered for pressure force in x-direction for RANS results. The magnitude and trajectories from laminar results of pressure forces in both x- and z-directions resembles the results from PANS simulation. Both laminar and PANS simulations captured a a local minimum trend in the pressure force in z-direction in Figure 5.11 between two consecutive maximum. In addition, the laminar simulation estimated larger maximum and lower minimum pressure force in z-direction comparing to PANS results.

The summation of pressure forces and viscous force in x- and z-directions respectively were also proceeded to obtain lift and drag forces profiles for RANS and PANS simulations. Figure 5.13 shows the lift and drag force data obtained after summation of pressure and viscous forces respectively in x- and z-directions.

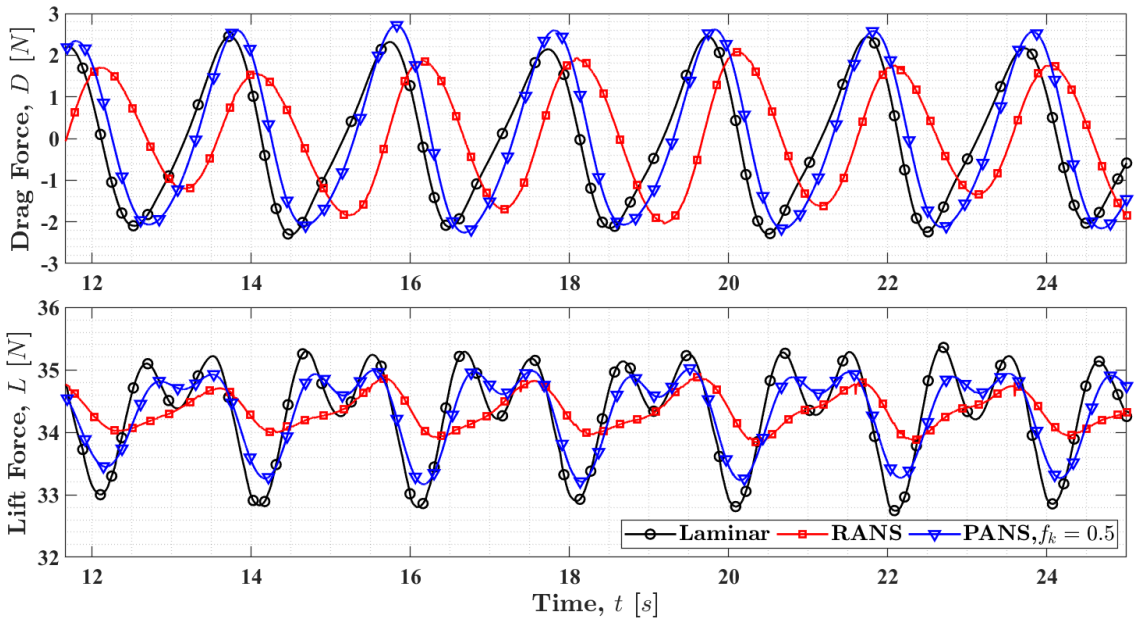

Figure 5.13: Profiles of lift and drag forces from Laminar, RANS, and PANS simulations

Due to the pressure force in z-direction showing dominating effect as explained in Section 5.3, the lift and drag force profiles from laminar, RANS, and PANS simulation shows almost identical trend in Figure 5.13 to Figure 5.11. Similarly, the discoveries in the pressure force comparison between the three simulations in Figure 5.11 are also reflected in Figure 5.13.

The mean values are computed again or both RANS and PANS results for comparison. Since the buoy is constrained to heave motion only, the mean calculation is only conducted for lift data. Moreover, the magnitude of drag force reflected in Figure 5.13 is much smaller than that of the lift force, which is another reason for the drag force comparison to be ignored. The mean lift force from PANS results are calculated to be 34.35 [N], which is also used as a reference for Laminar and RANS results to compare to. Table 5.4 shows the results of this comparison.

Table 5.4: Mean lift force comparison to PANS simulation results for both laminar and RANS methods

Simulation Approach	**Mean Lift Force [N]**	**Percentage Difference**
Laminar	34.18	0.495%
RANS	34.46	0.320%

The comparison results show a close match of the mean lift force for all three numerical simulations. The laminar and PANS simulations show similar profile shape of the lift force, capturing both the primary and secondary modes of the dynamic forces (lift force). Even if the mean lift results from RANS results showed low percentage difference comparing to laminar and PANS simulations, the failure in capturing the secondary modes in the lift profile thus displaying trajectories with large disparities from the laminar and PANS simulations indicated accuracy problem for RANS scheme in solving this problem.

5.5.3 Computational Cost Comparisons

With the accuracy evaluation for results from laminar, RANS, and PANS simulations accomplished, the last comparison features the balance between the desired accuracy level and the computational power requirement. For the laminar simulation in this research, numerical errors are discovered in force measurement (Section 5.3) and in heave motion prediction (Section 5.2.1) due to the increased cell skewness during the motion of the buoy. However, the simulation execution time is as low as 4 hours, which makes this approach very appealing in solving this 2-phase incompressible flow with floating buoy constrained to heave motion only. On the other hand, with more thorough understanding of the mechanisms of mesh refinement technique as well as the Savitzky-Golay data filtering technique in the post-processing, it is very probable that these accuracy issues can be resolved.

When it comes to the PANS scheme, the complex filter used during the simulation lead to an overwhelming computational power requirement. Even if the overall accuracy level of the results compared to the data from Experiment 2 in heave motion (Figure 5.10 and Table 5.3), the scheme appears to be computational demanding and the simulation execution time was as long as 3 days. Moreover, another attempt to improve the accuracy by using more complex result filters was initiated by the members of Fürth Lab. The simulation only covered 5 $[s]$ in 2 days after execution, leading to a rough estimation of 10 days for the simulation to finish. In this way, this attempt was terminated and the results will not be discussed in this thesis.

As for RANS scheme on this problem, serious accuracy problems are discovered for both heave motion estimation in Figure 5.10 and force measurements in Figures 5.11 and 5.13. More importantly, the RANS scheme simulation execution time was even longer than that of laminar simulation at some 9 hours, which disqualifies this scheme for solving this problem in this research.

6. CONCLUSIONS

In this study, a laminar simulation of the dynamic response of a heaving buoy, subject to non-linear second-order Stokes waves, was conducted. The wave field was simulated first without the involvement of the floating buoy and compared to a control experiment for validation. A mesh independence test was conducted for seven different mesh designations. This indicated convergence for the chosen intermediate mesh, with low percentage difference among different mesh conditions. The results from the simulation with the buoy involvement contains pressure and viscous forces in x, y, and z direction. Additional heave and velocity profiles are also compared to experimental results for validation and analyzed together with simulation results using RANS and PANS methods.

The wave modelled without buoy involvement is successfully validated by the data from control experimental with low percentage difference in mean peak and trough amplitude and even matching mean wave heights. Some unexpected small changes in the wave shape during the initial stage from 4 [s] to 6 [s] in the wave times series (see Figure 5.1) at early stages of the simulation were discovered. This is concluded to be due to transient behaviors with no recurrence at later time. A small scale frequency difference was also observed when comparing time series of waves generated using simulation results and experimental results. The cause is suspected to be experimental error in the manual settings of the wave frequency.

For the heaving buoy simulation, the force analysis indicated dominating pressure force compared to negligible viscous force. From the summation of pressure force and viscous force, it is discovered that the buoy is mainly affected by a large scale lift force and a smaller drag force. This is expected when the pressure force in z-direction is much larger than the pressure force in x-direction as was shown in Figure 5.6.

The heave motion profile is successfully validated by the data from previous experiments. Overall, the laminar simulation showed a high success in estimating both the heave motion and the exerted lift force on the buoy due to incidental waves. This observation is made in comparison with the previous experiment data and PANS simulation. An anomaly was found with the mean of the minimum heave magnitude from simulation showing a 22.7% error comparing to the experimental data. This is likely due to the problem of increased skewness in cells, when the buoy is at minimum heave. A possible solution to reduce this error involves increasing mesh density.

Mesh refinement was attempted in order to fix both the relatively large percentage errors discovered in mean minimum heave and the jump of data discovered in time series of pressure and lift forces in z-direction. Due to lack of time, and limited understanding of the mechanisms of mesh refinement, the results showed decreased wave heights as well as decreased heave magnitude. Moreover, the simulation time increased to almost 4 times that of previous design and was not used for this study.

The data jump was eventually resolved by applying the Savitzky-Golay data smoothing techniques. However, this method remains controversial. Firstly, the principles based on which the frame length and order of convolution are not well defined in any historical researches. In this way, these two parameters used in the data smoothing process in this research were determined merely by visual judgement of the smoothing outcomes after multiple different combinations of frame lengths and orders of convolutions were attempted. Secondly, [25] commented editorially that using data smoothing in numerical simulations lies in a murky area since many researchers proposed the possibility of data distortion when using this technique. Yet, this data smoothing technique worked in this study and is thus used during numerical error correction. The outcomes indicated identical graphical representation as well as mean lift force value.

The balance between desired accuracy level and the computational cost between different sim-

ulation method (laminar simulation, RANS, and PANS) were evaluated. The laminar simulation required the lowest computational power and finished the simulation in 4 hours while some numerical errors are discovered. However, these errors can be potentially fixed once mesh refinement is applied to improve mesh resolution locally to resolve increased cell skewness during buoy motion. The results from PANS scheme showed the highest overall accuracy yet the high computational power requirement lead to a long execution time of 3 days, which makes this approach not as practical as the laminar simulation in this problem. The RANS approach took 9 hours to finish the simulation, which indicates higher computational power requirement compared to the laminar simulation while lower requirement compared to PANS scheme. However, the results from RANS simulation showed large errors, thus disqualified for solving this problem.

6.1 Future Works

In future extensions to this study, the numerical damping approach will be examined by applying a regionally denser mesh around the still water level to obtain more accurately captured free surface elevation data to resolve the dissipation problem illustrated in Figure 4.3. The significance of this proposed improvement lies in the potential to shorten the extended wave tank. The majority of the computational power could be spent in the measurement zone if the wave was successfully damped at the outlet to prevent reflective waves. This could reduce the computational time required. Alternatively, the simulation time can possibly be extended for more comprehensive comparisons.

More investigation into the mesh refinement mechanism is required to increase the accuracy of the heave motion of the buoy. This could resolve the relatively large percentage error in mean minimum heave comparing to the experiment. In combination with the mesh refinement, new inner and outer distance of the mesh around the buoy can be designed to allow more "free space" for the buoy motion so that the increased cell skewness will not be serious enough to degrade the accuracy.

More systematical studies of the Savitzky-Golay filtering should be conducted in order to understand the principle of frame length and order determination. In detail, previous researches found correlation between these parameters and the overall main signal and noise signal frequencies [29, 15]. To investigate such correlations, different combinations of frame length and order of convolution can be tested within given main signals corrupted by different frequencies of small noises.

REFERENCES

[1] BUELOW, P., VENKATESWARAN, S., AND MERKLE, C. L. Effect of grid aspect ratio on convergence. *AIAA journal 32*, 12 (1994), 2401–2408.

[2] BUI, T. Explicit and implicit methods in solving differential equations.

[3] CHEN, L., SUN, L., ZANG, J., AND HILLIS, A. Numerical simulation of wave-induced roll of a 2-d rectangular barge using openfoam.

[4] COURANT, R. Courant-friedrichs-lewy condition.

[5] COURANT, R., FRIEDRICHS, K., AND LEWY, H. On the partial difference equations of mathematical physics. *IBM journal of Research and Development 11*, 2 (1967), 215–234.

[6] DEAN, R. G., AND DALRYMPLE, R. A. *Water wave mechanics for engineers and scientists*, vol. 2. world scientific publishing company, 1991.

[7] DESHPANDE, S. S., ANUMOLU, L., AND TRUJILLO, M. F. Evaluating the performance of the two-phase flow solver interfoam. *Computational science & discovery 5*, 1 (2012), 014016.

[8] GOMES, M. D. N., ISOLDI, L., OLINTO, C., ROCHA, L., AND SOUZA, J. Computational modeling of a regular wave tank. In *2009 3rd Southern Conference on Computational Modeling* (2009), IEEE, pp. 60–65.

[9] GOPALA, V. R., AND VAN WACHEM, B. G. Volume of fluid methods for immiscible-fluid and free-surface flows. *Chemical Engineering Journal 141*, 1-3 (2008), 204–221.

[10] HADDADI SISAKHT, B., JORDAN, C., AND HARASEK, M. Openfoam® basic training, 2019.

[11] HAMADA, A. A., AND FÜRTH, M. Numerical simulation of the effect of buoy geometries on pto of wave energy converters. In *SNAME Maritime Convention* (2021), OnePetro.

[12] HAMADA, A. A., ROLEN, A., MCCULLOUGH, W., AND FÜRTH, M. Numerical simulation of the effect of wave characteristics on pto of point absorber wave energy converter. In *SNAME 27th Offshore Symposium* (2022), OnePetro.

[13] HAMADA, A. A. A. A. private communication, May. 2022.

[14] HIRT, C. W., AND NICHOLS, B. D. Volume of fluid (vof) method for the dynamics of free boundaries. *Journal of computational physics 39*, 1 (1981), 201–225.

[15] KAKKAR, D., ET AL. Accounting for order-frame length tradeoff of savitzky-golay smoothing filters. In *2018 5th International Conference on Signal Processing and Integrated Networks (SPIN)* (2018), IEEE, pp. 805–810.

[16] KLEEFSMAN, K., FEKKEN, G., VELDMAN, A., IWANOWSKI, B., AND BUCHNER, B. A volume-of-fluid based simulation method for wave impact problems. *Journal of computational physics 206*, 1 (2005), 363–393.

[17] KOO, W.-C., KIM, M.-H., AND RYU, S. The function of computer utilization in educating and researching ocean engineering problems. *Journal of Ship and Ocean Technology 12*, 4 (2008), 1–6.

[18] KUNDU, P. K., COHEN, I. M., AND DOWLING, D. R. *Fluid mechanics*. Academic press, 2015.

[19] LANEY, C. B. *Computational gasdynamics*. Cambridge university press, 1998.

[20] LE MÉHAUTÉ, B. *An introduction to hydrodynamics and water waves*. Springer Science & Business Media, 2013.

[21] LEE, M., PARK, G., PARK, C., AND KIM, C. Improvement of grid independence test for computational fluid dynamics model of building based on grid resolution. *Advances in Civil Engineering 2020* (2020).

[22] LIU, X., AND GARCIA, M. H. Three-dimensional numerical model with free water surface and mesh deformation for local sediment scour. *Journal of waterway, port, coastal, and ocean engineering 134*, 4 (2008), 203–217.

[23] OPENFOAM, O. The open source cfd toolkit user guide. *OpenFOAM Foundation, Dordrecht* (2012).

[24] PILLIOD JR, J. E., AND PUCKETT, E. G. Second-order accurate volume-of-fluid algorithms for tracking material interfaces. *Journal of Computational Physics 199*, 2 (2004), 465–502.

[25] PRESS, W. H., AND TEUKOLSKY, S. A. Savitzky-golay smoothing filters. *Computers in Physics 4*, 6 (1990), 669–672.

[26] RANSLEY, E. J. Survivability of wave energy converter and mooring coupled system using cfd.

[27] RENARDY, M., RENARDY, Y., AND LI, J. Numerical simulation of moving contact line problems using a volume-of-fluid method. *Journal of Computational Physics 171*, 1 (2001), 243–263.

[28] REYNOLDS, O. Xxix. an experimental investigation of the circumstances which determine whether the motion of water shall be direct or sinuous, and of the law of resistance in parallel channels. *Philosophical Transactions of the Royal society of London 174* (1883), 935–982.

[29] SADEGHI, M., AND BEHNIA, F. Optimum window length of savitzky-golay filters with arbitrary order. *arXiv preprint arXiv:1808.10489* (2018).

[30] SALLAM, O., FENG, R., STASON, J., ROLEN, A., RODRIGUEZ, I., FÜRTH, M., ET AL. Computer vision techniques for floating structures experimental analysis: A heaving buoy case study. unpublished.

[31] SENG, S., MONROY, C., AND MALENICA, S. On the use of euler and crank-nicolson time-stepping schemes for seakeeping simulations in openfoam. In *MARINE VII: proceedings of the VII International Conference on Computational Methods in Marine Engineering* (2017), CIMNE, pp. 905–920.

[32] TIAN, X., WANG, Q., LIU, G., DENG, W., AND GAO, Z. Numerical and experimental studies on a three-dimensional numerical wave tank. *IEEE access 6* (2018), 6585–6593.

[33] WINDÉN, B. An Open-Source Framework for Ship Performance CFD. In *SNAME Maritime Convention* (04 2021), vol. Day 2 Wed, April 07, 2021. D021S003R002.

[34] WINDÉN, B. Predicting the Powering Performance of Different Vessel Types using an Open-Source CFD Propulsion Framework. In *SNAME Maritime Convention* (10 2021), vol. Day 2 Thu, October 28, 2021. D021S004R004.

APPENDIX A

Existing Validation Data

Previous existing experimental results [30] has been used for further evaluation. Since their paper is not published yet, their set up is described in detail here. Two resistance type wave gauges were installed at 3.16 [m] and 4.53 [m] from the upstream end of the tank for surface elevation measurements. Another depth camera was installed upstream with a tilt angle to record surface elevation. The water surface was covered in white foam balls to improve the performance of the stereo vision depth camera. In the mid-point of the two wave gauges, a buoy constrained to heave motion only was installed at 3.85 [m] of the tank. The buoy was 0.17 [m] in diameter and 0.26 [m] in height with a total weight of 3.5 [kg]. Moreover, the same beach made of porous material with height of 0.6 [m] and base of 1.2 [m] was installed at the far end of the wave tank accounting for wave absorption.

Figure A.1 shows a schematic view of the physical experiment setup with all measurements in [mm]. The motion of the buoy was captured by a camera, mounted normal to the transparent tank side wall using Visual Simultaneous Localization and Mapping (VSLAM) algorithm as well as by an Inertial Measurement Unit (IMU) mounted on top of the buoy.

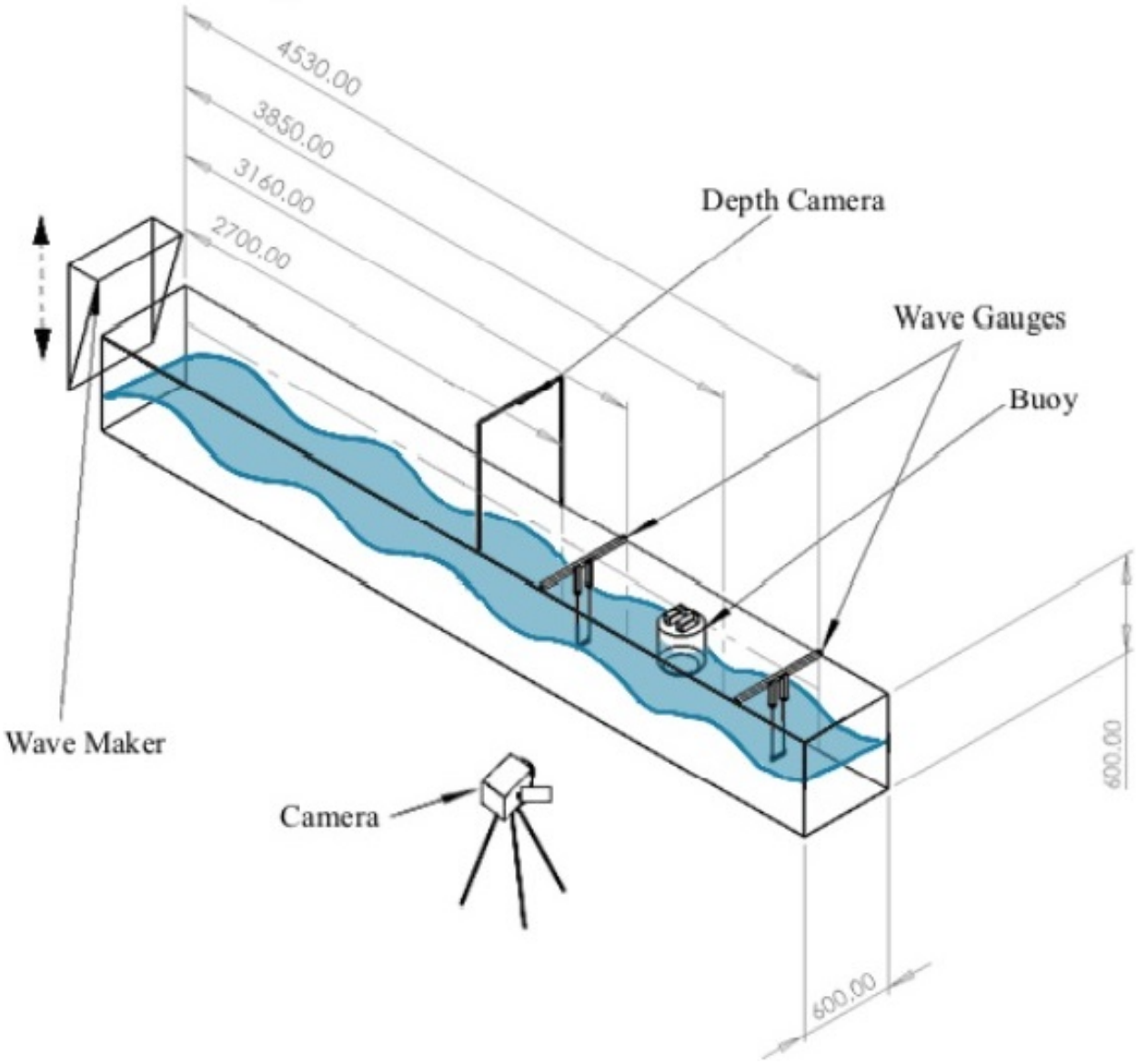

Figure A.1: Isometric View of Experimental Setup (Units:mm).

The incident wave for the experiment was 0.047 $[m]$ in wave height and a period of 2 $[s]$. According to Equations 2.5, 2.6a, 2.6b, and Figure 2.2, the wave is classified as a nonlinear second order Stokes wave which features narrower higher peak amplitudes as well as wider smaller trough amplitudes. In other words, the wave amplitude is not half of the wave height (0.024 $[m]$) as in the case in Airy wave theory and the amplitude is calculated using Equation 2.5, 2.6a, and 2.6b to be 0.027 $[m]$.